1 Geostrophic circulation and tidal effects in the Gulf of Gabès

- 2 Maher Bouzaiene¹, Antonio Guarnieri^{1,8}, Damiano Delrosso¹, Ahmad F. Dilmahamod², Simona
- 3 Simoncelli¹, Claudia Fratianni¹
- ⁴ Istituto Nazionale di Geofisica e Vulcanologia, Sezione di Bologna, Viale Berti Pichat 6/2, 40127,
- 5 Bologna, Italy
- 6 ²GEOMAR Helmholtz Centre for Ocean Research Kiel, Wischhofstr 1-3, 24148 Kiel, Germany
- 7 anow at: DG MARE European Commission, 1049, Brussels, Belgium
- 8 Correspondence to: Maher Bouzaiene (maher.bouzaiene@ingv.it)
- 9 **Abstract.** The mean kinematic features in the Gulf of Gabès region are analyzed based on 30 years
- of altimetry data (1993-2022) and the outputs of a high resolution ocean model for the year 2022. A
- 11 comparison of the seasonal variability in three different geographical areas within the gulf is
- 12 presented. In the northern and southern parts of the gulf, anticyclonic structures prevail, while the
- 13 central area is dominated by divergence. Similarity in flow topology is found in these three areas of
- 14 the gulf due to the signature of hyperbolic regions. In winter and fall, the mean flow is oriented
- northward, while it is reversed in spring and summer. The tidal perturbations influence sea level,
- 16 kinetic energy and hyperbolic geostrophic structures, leading to the generation of a cyclonic current
- in the central part of the gulf and to the presence of persistent strain gradients amplifying hyperbolic
- 18 structures. The Finite Time Lyapunov Exponent (FTLE) computed using altimetry data highlights
- 19 the link between physical and biogeochemical dispersion, with the Gulf of Gabès mean circulation
- 20 features acting as transport barriers for phytoplankton dispersion.

21 1 Introduction

- 22 Tidal forcing plays a crucial role in ocean circulation, and the Gulf of Gabès (GG) is notably
- 23 influenced by this phenomenon. Understanding tidal interactions with complex dynamics and their
- 24 impact on the transport of passive and active tracers (such as pollutants and marine species) is
- 25 challenging (Meyerjürgens et al, 2020). Well-known as a region of relevant tides within the
- 26 Mediterranean Sea (Abdennadher and Boukthir, 2006) with a semi-arid climate, high temperature,
- 27 relatively high salinity and strong density gradients, the GG is located in the southern part of the

28 Sicily Channel and represents a site of water masses exchange between the western and the eastern 29 Mediterranean Sea basins. 30 The gulf is considered one of the richest areas of the Mediterranean Sea in terms of nutrients 31 availability and biological production (Béjaoui et al., 2019; Ben Ismail et al., 2022; Salgado-32 Hernanz et al, 2019). Due to the gentle slope of its continental shelf and its shallow depth (Figure 33 1), the GG has the highest tidal range (with differences between high and low tides up to almost 2 34 m) in the Mediterranean Sea, is one of the areas in the Mediterranean Sea where the highest tides 35 can be found (Othmani et al., 2017) which strongly influences its circulation (Abdennadher and Boukthir, 2006; Sammari et al., 2006; Poulain and Zambianchi, 2007). Apart from the tides, 36 37 anticyclonic winds are also one of the drivers of the GG circulation (Sammari et al., 2006). 38 Originated from the Atlantic Water (AW), the Atlantic Tunisian Current (ATC) and the Bifurcation 39 Atlantic Tunisian Current (BATC) are the strongest surface currents evolving in the gulf (Ben Ismail 40 et al., 2015), while the Atlantic Ionian Stream (AIS) is generated by current instability and 41 topography (Menna et al., 2019), and it flows North of Malta island without penetrating in the GG 42 (Figure 2a) (Pinardi et al., 2015; Bouzaiene et al., 2020). The ATC is a permanent surface current characterized by low salinity (Sammari et al., 1999). It crosses the Strait of Sicily and circulates 43 along the Tunisian coast (Sorgente et al., 2011) where it splits into two branches. One of them 44 interests the coastal strip and flows in a southwesterly direction (Ben Ismail et al., 2010). Due to 45 its lower salinity, ATC branch circulates further offshore from the coast in a south-eastern direction 46 47 where it eventually follows the Libyan plateau (Figure 2a) (Millot and TaupierLetage, 2005). This 48 branch, observed especially in winter, is called the Atlantic Libyan Current (ALC). It circulates 49 along the Libvan shelf break where the mean flow is represented by a weak current bounded by a cyclonic vortex referenced as the Libyan Shelf Break Vortex (LSBV, Sorgente et al., 2011, see 50 51 Figure 2a). The BATC continues to circulate offshore, generating the Medina Gyre (MG) and the Southern Medina Gyre (SMG) (Figure 2a), whose formation is due to current instability or/and 52 53 topography (Jouini et al., 2016, Menna et al., 2019). Some efforts have been made to focus on the 54 dynamics of offshore waters in the central Mediterranean Sea from satellite-derived products i.e. the 55 dynamics in Sicily Channel show multi-scale spatial and temporal variability (Menna et al, 2019). Nevertheless, a long term analysis for understudied regions like the coastal GG areas can benefit an 56 57 overview of: persistent Lagrangian structures, attracting and repelling coastal zones, trends and 58 upwelling flows. 59

The GG dynamics are characterized by small and large-scale inter-annual and seasonal variability in the surface layer (Jebri et al., 2016). This system is identified by many spatio-temporal structures interacting with each other and producing an extremely complex and variable circulation.

60

62 Currents, filaments and eddies are responsible for water mass transport, thus the understanding of 63 their seasonal and inter-annual variability is crucial for a wide variety of reasons, such as regional 64 water exchanges with the open sea, large scale turbulent flow spreading, propagation of particles 65 and dispersion of sediments in the coastal zones. This is even more important in the GG 66 environment where the anthropogenic pressure has dramatically increased due to coastal phosphate processing plants by-products, frequent oil spill episodes, general pollution factors such as floating 67 68 marine debris or plastic, micro and macro litter (Ben Ismail et al., 2022). In addition, Lagrangian 69 studies on the transport of nutrients, jellyfish, eggs, and larvae would benefit from a better 70 knowledge of the mean circulation variability. To provide a realistic study for the GG circulation it 71 is necessary to evaluate in detail the long-term variability and the influence that tidal forcing, 72 interacting with topography, acts on the system, resulting in the generation of new structures 73 influencing turbulence and circulation in the entire gulf. 74 It has been shown in Elhmaidi et al. (1993) that turbulent features induce a discrepancy between

75 modeled and theoretical dispersion laws in case of two-dimensional turbulent dispersion theory for 76 isotropic and homogeneous flow. Two anomalous absolute dispersion (5/3, elliptic) and (5/4, hyperbolic) power laws were found in previous studies (Bouzaiene et al., 2021). These anomalous 77 regimes have been related to the sea topology through the presence of elliptic and hyperbolic 78 79 structures (Bouzaiene et al., 2018, 2021). In the eddy inner parts, these areas are referred to as 80 elliptic regions characterized by high vorticity gradients, while hyperbolic features are detected in 81 the coherent structure outer parts and can be related to sheared/stretched ocean flow. In Gomez-82 Navarro et al., (2024) the impact of tidal forcing on surface particle transport is explored, while the influence of tidal perturbation on the dispersion of elliptic and hyperbolic regions lacks, in our 83 84 opinion, a certain degree of discussion. 85 To our knowledge, the impact of tides on topology (the distribution of elliptic and hyperbolic

regions) in the GG has not been studied before, even though tidal forcing is very important in this area. Hence, given their potential influence on phytoplankton blooms, nutrient distribution, and marine litter dispersion, it is essential to gain a better understanding of how tides influence the circulation, dynamics, and sea topology. Altimetry data analysis allows analyzing the geostrophic circulation and the kinematic properties of mesoscale structures.

However, their low temporal and spatial resolutions do not allow performing a realistic study on the dynamics introduced by tides. In order to address this issue, we leveraged high temporal resolution (hourly) model outputs from a numerical system which includes tides.

In this study, we focus on the kinematic properties of the geostrophic component of the circulation in the GG and on how tides affect currents. We do this by using altimetry data covering the time

- period 1993-2022 and model analysis data for the year 2022, both distributed by the Copernicus 96 97 Marine Service (CMS, http://marine.copernicus.eu/). Previously, some efforts to understand this oceanographic system have been made by focusing on the general aspects of the Gulf of Gabès 98 circulation (Ben Ismailet al, 2015, 2020; Zayen et al, 2020). The impact of internal waves on 99 100 mesoscale eddies is studied in Barkan et al., (2017, 2021) where the signal increases significantly when tidal forcing is present. Furthermore, the impact of the velocity fields from a high-resolution 101 102 coupled ocean—wave model simulation (Clementi et al, 2021) on simulated surface particle dispersal was studied in the Mediterranean Sea (Rühs et al, 2025). The comprehension of how tides 103 104 influence the geostrophic features is still an open question.
- Our aim is to investigate new features of the geostrophic circulation and to assess the impact of tides on the geostrophic circulation. High-resolution ocean circulation modeling and satellite altimetry could enhance our understanding of the geostrophic transport. The paper is organized as follows: in section 2 we describe the datasets used and the methods applied. The results on geostrophic structures from altimetry and model data are presented in section 3. Summary and conclusions are proposed in section 4.

2 Material and methods

112 **2.1 Datasets**

111

- 113 The geostrophic circulation in the GG has been investigated by means of remote-sensed altimetry
- data and outputs from a high-resolution oceanographic numerical system.

115 **2.1.1 Altimetry data**

- 116 The satellite altimetry dataset used in this study is a subset of the CMS
- 117 SEALEVEL_EUR_PHY_L4_MY_008_068 product (European Union-Copernicus Marine Service.
- 118 (2021), Mercator Ocean International, https://doi.org/10.48670/MOI-00141), with a spatial
- resolution of 0.125° × 0.125° and a daily temporal resolution. Our analyses were conducted over a
- 30-year period, from 1993 to 2022. For more details see the Quality Information Document (QUID)
- 121 (https://documentation.marine.copernicus.eu/QUID/CMEMS-SL-QUID-008-032-068.pdf). The
- variable used is the absolute surface geostrophic velocity and we inferred the vorticity, the
- divergence, the Okubo-Weiss parameter, the deformation gradients and the Finite Time Lyapunov
- 124 Exponent (FTLE) from the surface geostrophic velocity variable from the Absolute Dynamic
- 125 Topography (ADT). These parameters were investigated in order to elucidate the mean circulation,
- 126 persistent currents, eddies and gyres.

127 2.1.2 Chlorophyll-a data

- The 128 chlorophyll-a dataset used in this study is the **CMS**
- OCEANCOLOUR MED BGC L4 MY 009 144 product. We used the daily mass concentration 129
- of chlorophyll-a in sea water (CHL) at 1 km resolution from the Ocean Satellite Observations for 130
- multi-year Bio-Geo_Chemical (BGC) regional datasets (https://doi.org/10.48670/moi-00300). 131

132 2.1.3 Model data

- fields 133 Hourly Sea Surface Height (SSH) from model data (CMS
- 134 MEDSEA_ANALYSISFORECAST_PHY_006_013 (Clementi et al., 2021) covering the year 2022,
- 135 are used to compute geostrophic currents. We have chosen the year 2022 since at the time the
- 136 dataset was processed it was the only complete year for the CMS system including tidal signals in
- the hydrodynamic model used. The physical component of the Mediterranean Sea within the 137
- 138 framework of CMS (Med-Physics) is a tidal, coupled hydrodynamic-wave model with a data
- 139 assimilation system implemented over the whole Mediterranean Sea, and a horizontal resolution of
- 140 1/24° (~4 km) and 141 unevenly spaced vertical z* levels (Clementi et al. 2017). More detailed
- information on the system and its products can be found in the Quality Information Document 141
- 142 (https://catalogue.marine.copernicus.eu/documents/QUID/CMEMS-MED-QUID-006-013.pdf).

143 2.2 Methods

- To describe the kinematic properties and the circulation of the GG we estimated the geostrophic 144
- 145 currents for the vear 2022 from the model data
- (MEDSEA_ANALYSISFORECAST_PHY_006_013) SSH fields and we then computed the four 146
- 147 following quantities from the altimetry data and model data (described in section 2.1.1 and 2.1.3,
- 148 respectively): normalized vorticity (with respect to f), normalized divergence, normalized Okubo-
- 149 Weiss parameter and FTLE.

150 2.2.1 Estimation of the geostrophic currents

- 151 The model SSH field (section 2.1.3) was used to estimate the geostrophic currents, resulting from
- the balance between the Coriolis force and the horizontal pressure gradient. The zonal (ugeos) and 152
- 153 the meridional (vgeos) components of the geostrophic velocities are derived from the geostrophic
- 154 equations as follows (Apel, 1987; Vigo et al., 2018a; 2018b):

155
$$ugeos = \frac{\frac{-g}{f} \partial \eta}{\partial y} (1)$$

156 $vgeos = \frac{\frac{g}{f} \partial \eta}{\partial x} (2)$

156
$$vgeos = \frac{g}{f} \partial \eta$$
 (2)

- Where, x and y are the longitude and the latitude components respectively, η is the model SSH,
- 158 g=9.81 m/s² is the gravity acceleration, f=2 Ω sin(λ) is the Coriolis parameter, λ is the latitude in
- degrees and $\Omega = 2\pi/T$ is the Earth angular velocity, being T the period of rotation.
- 160 In order to evaluate the tidal residual from the full SSH signal, a Doodson filter was applied to the
- 161 dataset, following the approach proposed in the Manual on Sea Level Measurement and
- 162 Interpretation of the IOC (1985). The Doodson is a low-pass, symmetric filter based on the
- definition of 19 coefficients as follows:
- 164 F(t)=(2, 1, 1, 2, 0, 1, 1, 0, 2, 0, 1, 1, 0, 1, 0, 0, 1, 0, 1); F(t)=F(-t)
- The value of the de-tided sea level SSH_{res} at time t_0 is calculated as:

166
$$SSH_{res}(t_0) = \frac{1}{30} \sum_{d=-19}^{d=19} F(d) SSH(t_0+d); d \neq 0(3)$$

- Where SSH denotes the sea level elevation, t₀ is the time expressed in hours and the coefficients d
- represent the increasing or decreasing hours with respect to the central value t₀.
- 169 2.2.2 The normalized vorticity
- 170 The normalized vorticity which is equivalent to the Rossby number (Ro) and is defined as (Poulain
- 171 et al., 2023):

172
$$\zeta^* = \frac{\zeta}{f}$$
, $\zeta = \frac{\partial v}{\partial x} - \frac{\partial u}{\partial y}(4)$

- where ζ is the relative vorticity, ζ^* is a good indicator of features activity in the ocean. If $\zeta^*\sim O(1)$,
- the flow shows a-geostrophic features while for ζ^* <<1 the flow shows quasi-geostrophic structures
- 175 (Siegelman, 2020). For $\zeta^*>0$, indicates the presence of cyclonic structures, whereas when ζ^* is
- 176 negative the flow shows anticyclonic features.
- 177 **2.2.3** The normalized divergence
- 178 The normalized divergence, a fundamental metric to characterize the transport of passive and active
- 179 tracers, is defined as (Poulain et al., 2023):

180
$$\delta^* = \frac{\delta}{f}$$
, $\delta = \frac{\partial u}{\partial x} + \frac{\partial v}{\partial y}$ (5)

- where δ is the horizontal divergence of the velocity field. It allows us to detect two different
- dynamical oceanic zones: for $\delta^*>0$ (divergence) the flow fields tend to propagate outward through
- the surrounding surface of a closed control volume, diverging from its center, whereas for δ^* <0
- (convergence) the flow particles tend to converge to the center of the volume.
- 185 2.2.4 The normalized Okubo-Weiss parameter
- The normalized Okubo-Weiss parameter serves as a powerful indicator to distinguish between two
- different topological domains: elliptic or hyperbolic. It is defined as:

188
$$Q^* = \frac{(S^2 - \zeta^2)}{(S^2 + \zeta^2)}(6)$$

- Where S is the strain or rate of deformation of the flow and it is composed of a shear term S_s and of
- 190 a normal term S_n . It is defined as follow:

191
$$S = \left[S_s^2 + S_n^2\right]^{\frac{1}{2}} (7)$$

192 Where S_s and S_n are defined as

193
$$S_s = \left(\frac{\partial v}{\partial x} + \frac{\partial u}{\partial y}\right)^2$$
, $S_n = \left(\frac{\partial u}{\partial x} - \frac{\partial v}{\partial y}\right)^2$

- Where $Q^* = -1$ an elliptic domain can be defined, while where $Q^* = 1$ a hyperbolic region can be
- 195 identified (Okubo, 1970, Weiss, 1991, Elhmaidi et al., 1993; Bouzaiene et al., 2018, 2021). As
- shown by Bouzaiene et al. (2021), the flow dynamical properties in the eddy inner parts (elliptic
- regions) and surrounding coherent structures (hyperbolic structures) are very different. In this study
- 198 *S* is normalized by *f* to identify the sheared and/or stretched regions:

199
$$S^* = \frac{S}{f}(8)$$

200 2.2.5 The Finite Time Lyapunov Exponent

- 201 The Finite Time Lyapunov Exponent (FTLE) λ_t is a parameter which describes the separation
- amongst particles in a specific time interval and it has been used in several ocean applications to
- 203 identify the Lagrangian Coherent Structures (LCS) (Shadden et al., 2005; Farazmand and Haller,
- 204 2012; d'Ovidio et al., 2010; Rousselet et al., 2025). In previous investigations within the
- 205 Mediterranean region, the emphasis was on the Finite Scale Lyapunov Exponent (FSLE) rather than
- 206 the FTLE. The FSLE was calculated on the basis of the exponential growth of distances between
- 207 Lagrangian particle pairs initially separated. This calculation served the dual purpose of identifying
- 208 Lagrangian Coherent Structures (LCS), as demonstrated by d'Ovidio et al. (2004, 2009), and
- 209 comparing LCS with Lagrangian surface drifter trajectories, as explored by Bouzaiene et al. (2020).
- 210 More recently, Morales-Márquez et al. (2023) investigated the use of FSLE to characterize LCS
- 211 concerning mixing and transport properties in the upper layer of the entire Mediterranean Sea.
- Despite these advancements, the application of the parameter λ_t in coastal Mediterranean zones,
- 213 particularly in the GG, remains an unanswered question. The implementation of FTLE in coastal
- areas, namely from altimetry data, has been limited by the error of the data in very coastal areas.
- 215 This study seeks to address this gap by computing λt specifically for LCS analysis in these areas.
- The implementation of FTLE using particle trajectories with increasing resolution (Onu, et al, 2015)

- 217 in the GG could bring new insight into how coastal features impact biology. The use of FTLE in
- 218 coastal areas is reliable to detect LCS (Peng et al, 2024)
- 219 FTLE is a local scalar that represents the separation rate of initially neighboring particles for a finite
- 220 time [t_0 , t_0+T]. At position x_0 and time t_0 , λ_t is defined as follows (Haller, 2002, 2015; Liu et al.,
- 221 2018):

222
$$\lambda_{t}(x_{0}, t_{0}, T) = 0.5 \left[\frac{\log \lambda_{max} \left(\left[\frac{\partial \Phi(x_{0}, t_{0} + T, t_{0})}{\partial x_{0}} \right]^{tr} \left[\frac{\partial \Phi(x_{0}, t_{0} + T, t_{0})}{\partial x_{0}} \right] \right)}{T} \right] (9)$$

- where λ_{max} is the largest eigenvalue of the Cauchy-Green stress tensor, while the flow field of fluid
- particle trajectories is defined as $\Phi(x_0, t_0 + T, t_0)$ and tr indicates the matrix transpose.
- 225 In 2D turbulence theory, the eigenvalues of the Cauchy-Green tensor quantify the stretching of fluid
- 226 particles along their relevant directions (Liu et al., 2018). FTLE can be implemented forward-in-
- 227 time and/or backward-in-time and the implications for phytoplankton as one shows attracting and
- 228 the other repelling structures. In this work, we compute the forward-in-time or positive-time (T>0)
- of the λ_t field. This eigenvector is called "forward Finite-Time Lyapunov Vector". It has been shown
- 230 that λ_t is predominantly reliable to capture coherent structures starting from an integration time of 6
- days, with no upper limit (Du Toit, 2010; Rypina et al., 2011; Liu et al., 2018). In this study, daily
- FTLE fields are computed, and then averaged seasonally over a 30-year period to detect the mean
- 233 features and over 7 days to compare it to phytoplankton blooms occurring in GG. Here, λt is
- 234 calculated from the velocity fields derived from satellite altimetry data at temporal and spatial
- 235 resolutions of 1 day and 1/8°, respectively. Our choice is to set the resolution of the mean initial
- 236 trajectory conditions to 800 meters ×800 meters, corresponding to 1/128°, about 16 times larger
- than the velocity field resolution, which guarantees an LCS accurate enough for capturing oceanic
- 238 features (Onu et al., 2015). In general, high values of λt indicate the edges of coherent structures,
- 239 fronts and filaments (hyperbolic regions), while low values correspond to the inner parts of the
- 240 eddies (elliptic areas). Both are considered as transport barriers (Blazevski and Haller, 2014).
- 241 Intense stirring induced by strong turbulence disperses the high input of nutrients when uplifted
- 242 from deeper layers, whereas larger amounts of nutrients remain in more quiescent zones (decreased
- 243 turbulence; Hernandez-Garcia et al., 2010).



267

268

269

270

271

272

273

274

275

276

277

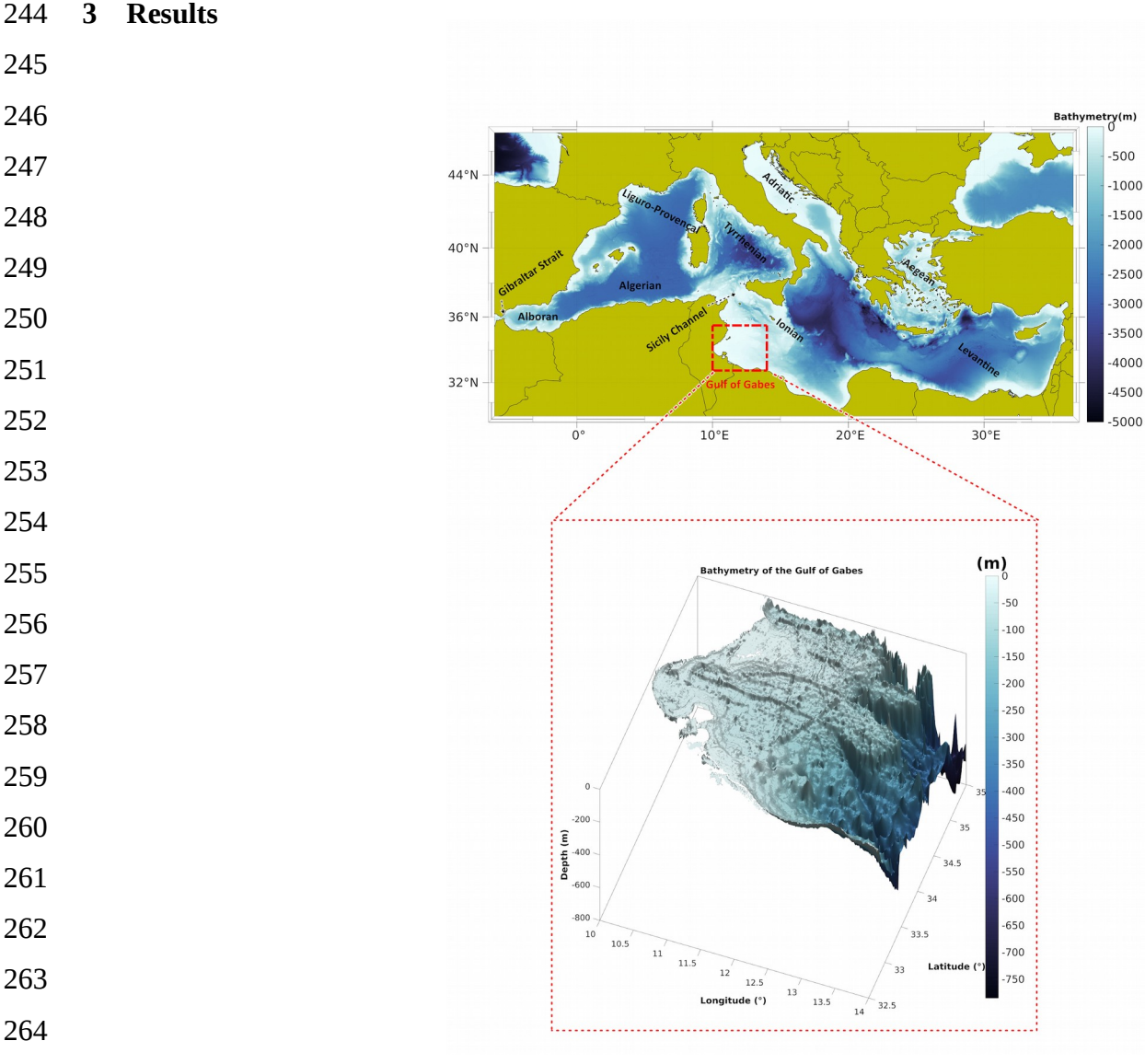


Figure 1: Bathymetry of the Mediterranean Sea with the main geographical sub-basins and straits locations. The red dashed rectangle in the upper panel shows the geographical limits of the larger Gulf of Gabès domain. A detail of 3D bathymetry in the Gulf of Gabès is shown in the lower panels. The bathymetry was derived from the Global Earth Bathymetric Chart of the Oceans for the 2022 version, with a spatial resolution of ~0.45 km (GEBCO_2022, https://www.gebco.net).

Three subareas were identified in the GG (black boxes in Figure 2) in order to highlight differences and similarities in the dynamical features: Northern Gulf of Gabès (NGG, 11°E-12°E and 34.6°N-35.25°N), Central Gulf of Gabès (CGG, 10°E-11°E and 33.75°N-34.4°N) and Southern Gulf of Gabès (SGG, 11.1°E-12.2°E and 33°N-33.75°N). The Mediterranean features are strongly driven by the instability of intense coastal currents, which have frequently changed their location and lifespan over the past decades (Bouzaiene et al, 2020; Poulain et al, 2012). In order to investigate the kinematic properties of mesoscale features, we used 30 years of altimetry data in the present paper, focusing on the main circulation features in the GG. This 30 year dataset allows for the detection of mean patterns across three decades, providing a basis to discuss the well-known mean features during the observational data availability period. The 30 years of satellite altimetry data are used to overview the mean kinematic features in the GG domain and in the three specified subareas, as detailed in section 3.1. The altimetry analysis could help to overview long term kinematic properties in the coastal regions (Rinivasan and Tsontos, 2023).

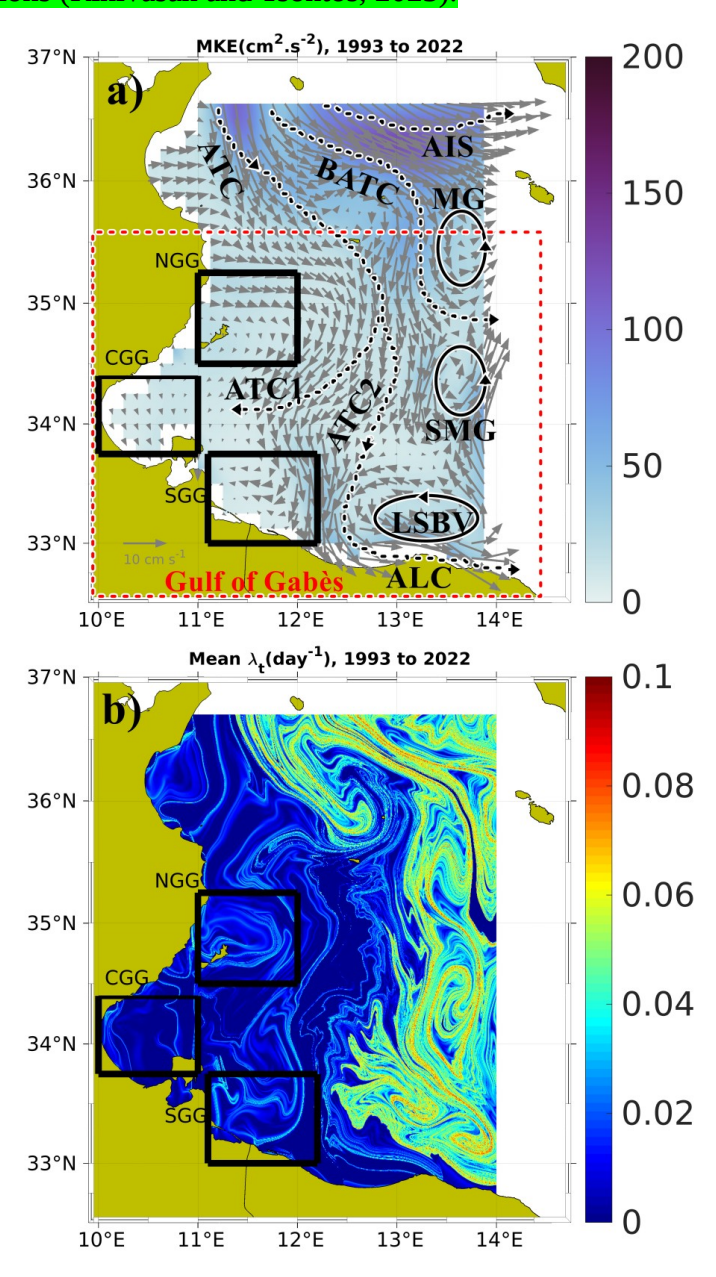


Figure 2: (a) Mean Kinetic Energy (MKE) with superimposed mean geostrophic currents estimated over the period 1993-2022; (b) Mean Finite Time Lyapunov Exponent (λ_i) computed from geostrophic velocities from altimetry data (SEALEVEL_EUR_PHY_L4_MY_008_068) in the same period. Three subareas are selected close to the coastal areas of the gulf as follows: NGG: Northern Gulf of Gabès, CGG: Central Gulf of Gabès, SGG: Southern Gulf of Gabès. List of acronyms of the main circulation features: MG: Medina Gyre, SMG: Southern Medina Gyre, LSBV, Libyan Shelf Break Vortex, ATC, Atlantic Tunisian Current, ATC1, First Atlantic Tunisian Current, ATC2: Second Atlantic Tunisian Current, ALC: Atlantic Libyan Current, AIS: Atlantic Ionian Stream, BATC: Bifurcation Atlantic Tunisian Current.

- 291 The relatively low temporal and spatial resolutions of the data do not allow us to make
- 292 considerations on the impact that tides have on GG features in a smaller area. Hence, we focused on
- 293 the GG Smaller Domain (CGG, 10.00°E-11.35°E and 33.40°N-34.75°N) where we derived
- 294 geostrophic currents from the SSH model fields allowing us to test the impact of tides in the GG, as
- 295 explained in section 3.2. SSH spatial and temporal averages in the CGG have been removed from
- 296 the native SSH fields.

- 297 The resulting mean seasonal geostrophic circulation in the CGG was compared to its counterpart
- 298 computed from the de-tided SSH fields, in order to assess the impact of tides on the geostrophic
- 299 dynamics of the Gulf. The de-tiding on the native SSH fields was performed using a Doodson filter
- 300 (see section 2.2.1 for details).

3.1 Altimetry data analysis of the mean geostrophic circulation

- 302 Figure 2a shows the geostrophic circulation (grey arrows) averaged over the period 1993-2022,
- 303 superimposed on the Mean Kinetic Energy $MKE = (0.5 | uaeos^2 + vaeos^2)$) for the same period,
- 304 where <...> represents the average over the 30 years. Several well-known structures are clearly
- 305 visible, namely: (1) the edges of the cyclonic features referenced as the Medina Gyre (MG), the
- 306 Southern Medina Gyre (SMG) and the Libyan Shelf Break Vortex (LSBV); (2) the first Atlantic
- 307 Tunisian Current (ATC1) which is well developed along the Tunisian coasts; and (3) the second
- 308 Atlantic Tunisian Current (ATC2), flowing near the Libyan boundaries and forming the Atlantic
- 309 Libyan Current (ALC), in agreement with the results of Sorgente et al. (2011), Jebri et al. (2016)
- 310 and Menna et al. (2019).
- 311 The MKE shows the presence of energetic features flowing into the GG as well as surrounding
- 312 eddies, BATC, ATC1 and ATC2 with MKE of ~50-100 cm²/s², while the Atlantic Ionian Stream
- 313 (AIS) inflows through the north-eastern Ionian Sea with a maximum MKE of approximately 100-
- 314 150 cm²/s². The mean FTLE averaged over the 30-year altimetry data period (λ_t ; Equation 9) is
- shown in Fig. 2b. λ_t can be applied to investigate the link between the GG dynamics and the
- 316 chlorophyll concentration, which are known to be related by inverse proportionality. The regions
- located far from the GG, are characterized by a large λ_t , close to 0.1 day⁻¹, indicating strong chaotic
- 318 advection clearly evidenced by the presence of intense eddies and persistent currents (MG, SMG,
- 319 LSBV, AIS, see Figure 2a vs. 2b). These features appear as local barriers to transport, inhibiting
- 320 biological production. On the contrary, in the coastal zones of the GG, λ_t tends to zero. These zones
- 321 may favor the nutrient standing stocks due to the weak effect of the horizontal mixing and stirring.
- 322 This could be one of the causes of the observed high chlorophyll concentration close to the Tunisian
- boundaries as shown in previous studies (Bel Hassen et al., 2010; Macias et al., 2018; Kotta et al.,

2019), where nutrients would flee from high turbulent zones to settle in less chaotic areas. We computed the daily mean speed and kinetic energy (KE) time series over 30 years (1993-2022) using altimetry data, as shown in Figure 3. The quantities are averaged over the larger GG box, indicated by the red rectangle in Figure 2. Higher speed and KE values are mostly observed in winter and fall, while lower values occur in spring and summer. This variability is likely strongly related to atmospheric forcing. In order to evaluate the evolution of regional dynamics over the decades, we computed the means of the two quantities separately for the three following periods: 1993-2002, 2003-2012 and 2013-2022. The mean speed increased over the decades, from 7.35 cm/s in 1993-2002, to 7.6 cm/s in 2003-2012, and 8.01 cm/s in 2013-2022. Similarly to the averaged speed, the Mean Kinetic Energy also increased by approximately 7 cm²/s² from the beginning to the end of the considered period.

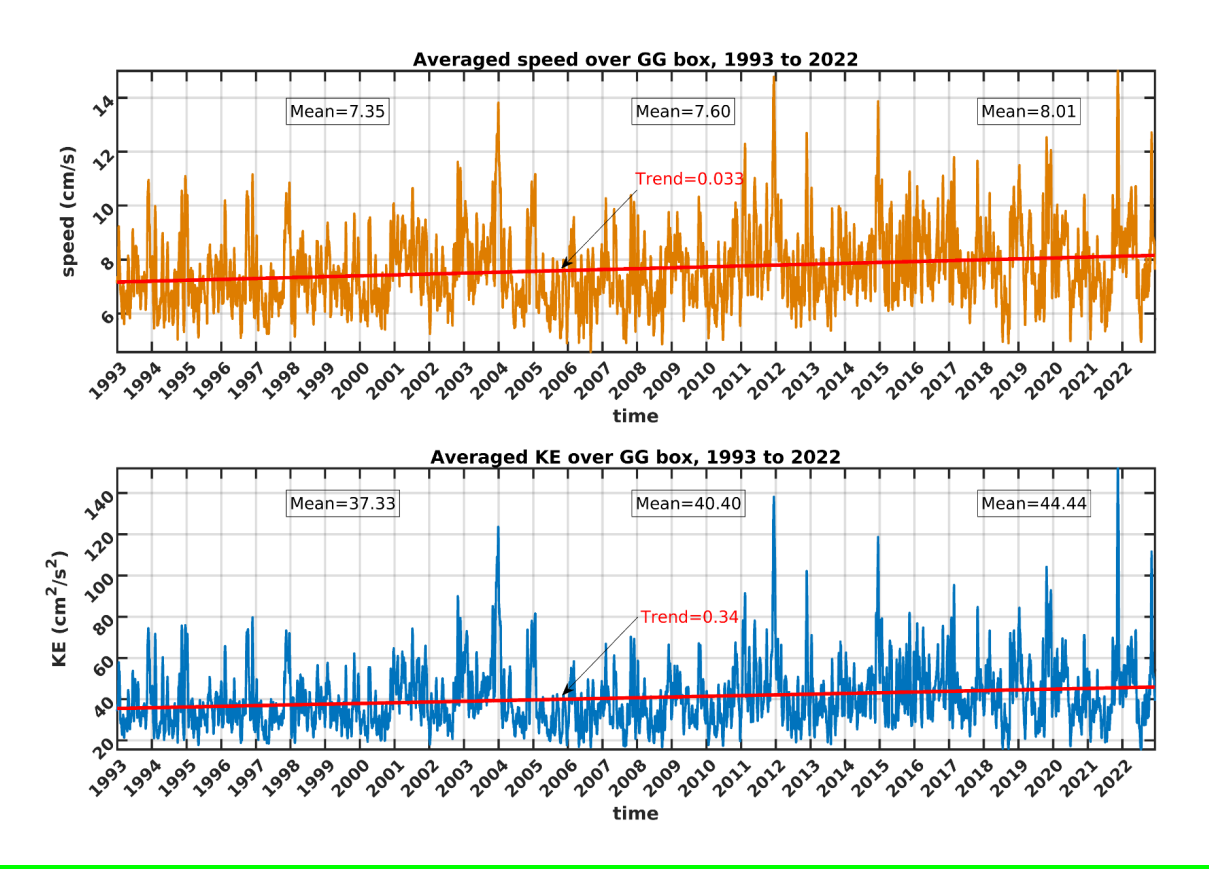


Figure 3: Time series of mean speed and Kinetic Energy estimated from geostrophic velocities provided by altimetry data (SEALEVEL_EUR_PHY_L4_MY_008_068) in the Gulf of Gabès over the period 1993-2022. The quantities are mean over the larger GG box as displayed with the red rectangle in Figure 2 a.

The NGG is clearly evidenced by the presence of a large anticyclonic current with $\lambda_t \sim 0$ in its core, while λ_t is greater than zero in the eddy outer part. A similar pattern can also be observed in the SGG. On the contrary, the mean FTLE in the CGG suggests the presence of filaments and fronts (Fig. 2b). Normalized vorticity (ζ^*), normalized Okubo-Weiss (Q*), normalized divergence (δ^*), and normalized deformation (S*) over the 30 years (1993-2022) from the altimetry product are

shown in Figure 4a,b,c and d, respectively, confirming the presence of the MG, SMG and LSBV eddies. Except for the MG, within the interior of these structures, the value of Q* is negative (elliptic regions) due to high vorticity gradients, whereas in the surrounding coherent structures the value of Q* is positive, with predominantly hyperbolic areas due to strong deformation gradients (Fig. 4b).

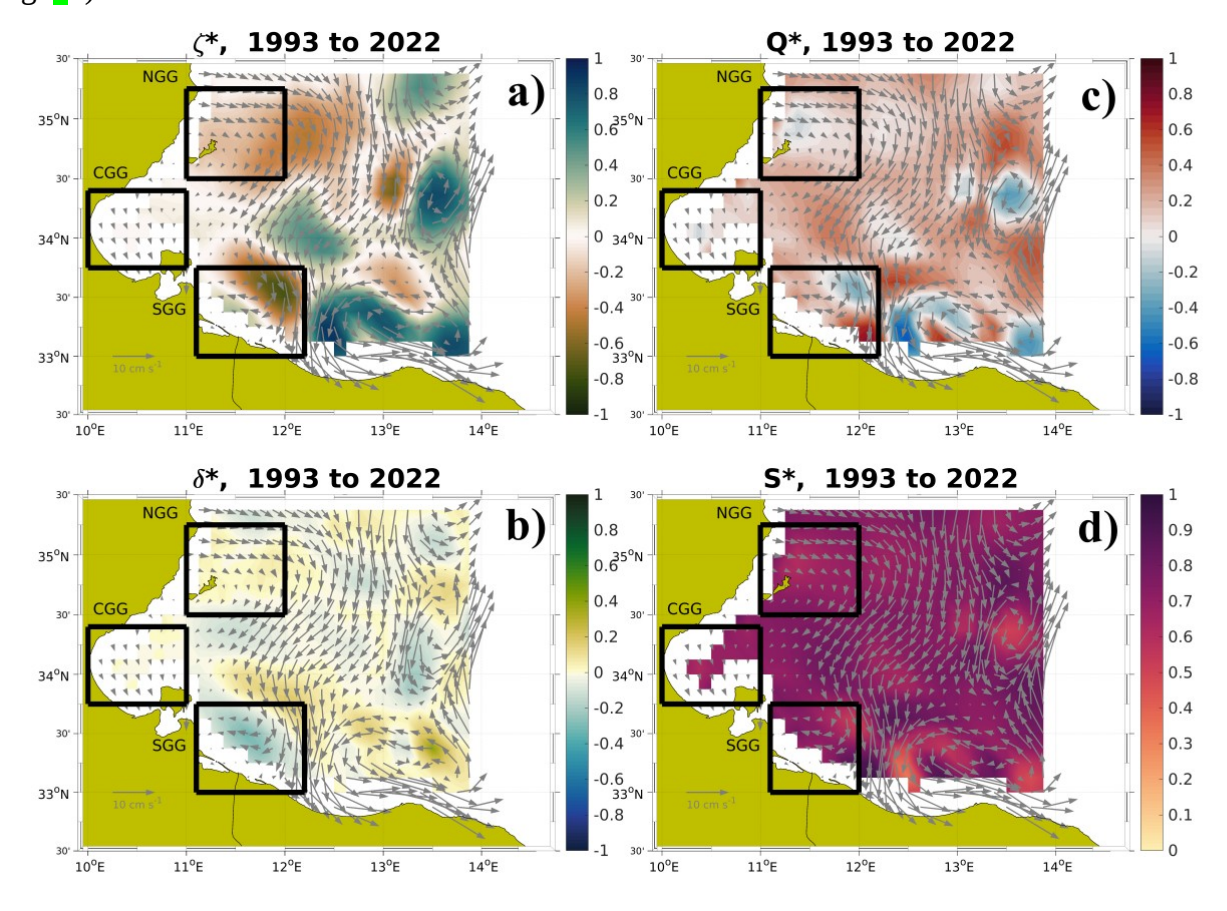


Figure 4: Mean circulation from altimetry data (SEALEVEL_EUR_PHY_L4_MY_008_068) estimated over the period 1993-2022 (a) Normalized vorticity (ζ^*), (b) normalized Okubo-Weiss parameter Q*, (c) the normalized divergence (δ^*) and (d) normalized deformation (S*) with superimposed mean geostrophic velocities. Three subareas are selected close to the coastal areas of the gulf as follows: NGG: Northern Gulf of Gabès, CGG: Central Gulf of Gabès, SGG: Southern Gulf of Gabès.

The vorticity mostly agrees with the divergence (Fig. 4a and c) for ζ^* and δ^* higher than zero, implying the presence of several permanent/recurrent eddies and gyres where the flow tends to propagate outward through the surrounding eddy cores (divergence). Upwelling of deep, nutrient-rich water masses occur in these areas, leading to enhanced biological production at the surface. In the opposite scenario (negative ζ^* and δ^*) the surface flow is pointing towards the inner parts of the anticyclonic eddy (convergence), pushing water towards its center of mass, then sinking to the bottom layers. The flow is sheared or stretched (S*~O(1)) in the eddy outer parts where the current is very unstable. These zones can be identified as hyperbolic regions due to strong deformation gradients, while for S*~0 (inside coherent vortices) the rotation is dominant (Figure 4 b and d). In

order to compare the dynamics of regions relatively close to the GG with farther ones, ζ^* , δ^* and Q* are seasonally evaluated in the three sub areas displayed in Figure 5. They can all be classified as hyperbolic regions (Q*>0, magenta lines in Figure 5) meaning that the flow can be stretched or sheared. Except for some seasons, the NGG and CGG surface waters tend to rotate into gyres (elliptic areas, Q*<0). In the CGG, the vorticity is oscillating from ~-0.5 (anticyclonic) to ~0.5 (cyclonic), while ζ^* shows mostly negative values in the two other areas considered (thus indicating the presence of anticyclonic vortices). In agreement with the vorticity values, the divergence is negative in the SGG (convergent flow, Fig 5c). In the NGG and CGG, δ^* indicates positive values, mostly greater than zero in the NGG, thus denoting the presence of upwelling flows (Fig. 5a,b blue line). The difference in the divergence of the three subareas might be related to the different interaction of the main forces (i.e. tides and winds) with the bottom topography.

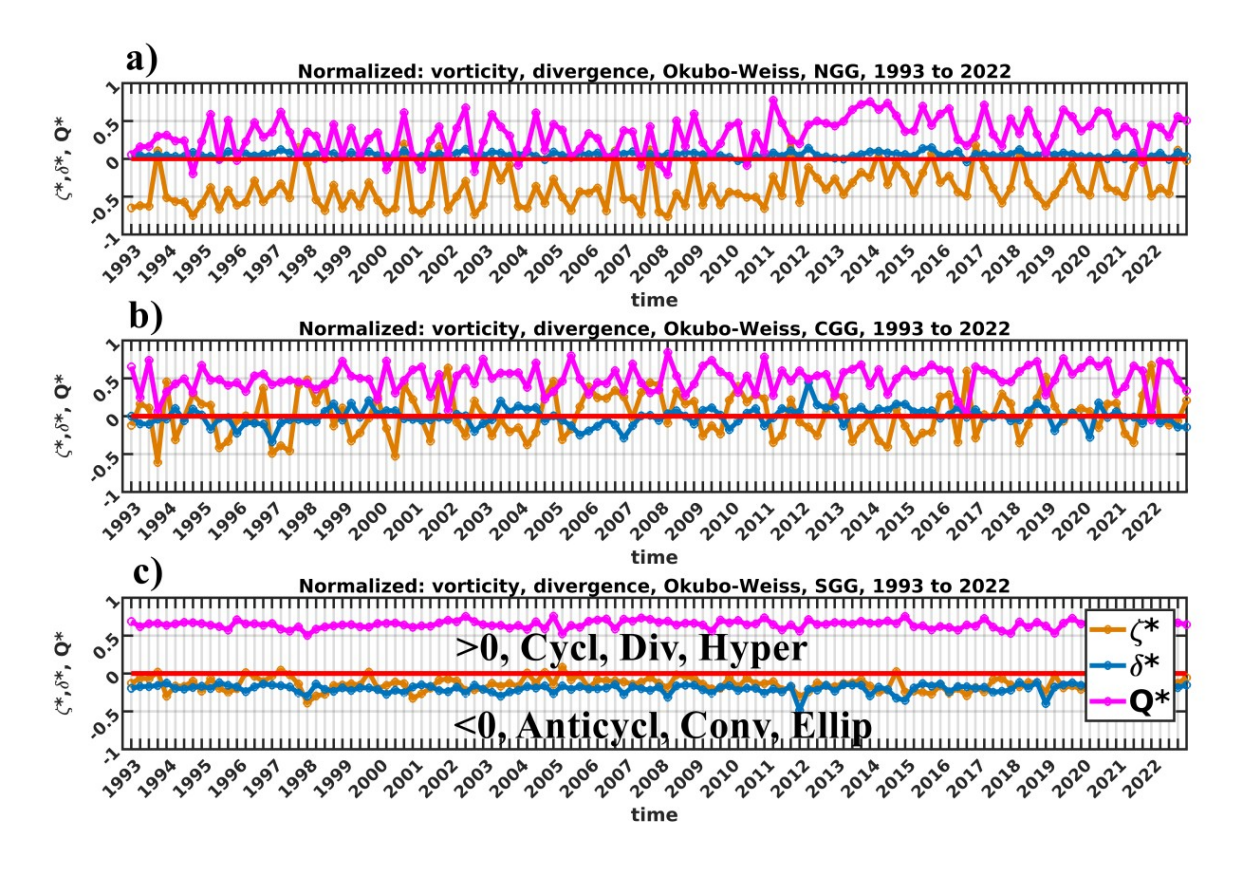


Figure 5: Time series of normalized vorticity (ζ^* ; yellow), normalized divergence (δ^* ; blue) and normalized Okubo-Weiss parameter (Q*, magenta) estimated from geostrophic velocities provided by altimetry data (SEALEVEL_EUR_PHY_L4_MY_008_068) in the Gulf of Gabès over the period 1993-2022. Panel (a): North GG; Panel (b): Central GG; Panel(c): South GG. The quantities are averages over each of the boxes defined in Figure 4.

3.2 Model data analysis of the geostrophic circulation in 2022

The GG surface circulation is strongly controlled by tides (Zayen et al., 2020). The highest tidal ranges can be detected in the central part of the GG, whilst they are much less significant outside of the gulf (Abdennadher and Boukthir, 2006). Tidal movements, which induce vertical mixing, could

383 be considered as a potential cause of high chlorophyll concentration in the CGG (Macias et al.,

384 2018).

385 The following sections will focus on the CGG dynamics, both because of its importance from the

386 biological production point of view, as shown previously by Feki-Sahnoun et al. (2018), and

387 because it represents a site of particular interest to investigate the influence of tidal forcing on

388 dynamics.

389

415

3.2.1 Seasonal variability

390 The comparison of the mean seasonal geostrophic circulation in 2022 derived from full SSH and 391 detided SSH is shown in Figures 6 and 7, where the arrows representing the geostrophic velocities are superimposed on the kinetic energy. During winter/fall the mean flow tends to inflow from the 392 393 south to the north, while in spring and summer its circulation is mainly cyclonic bordering the 394 coastline. Our results are in good agreement with previous studies in the Mediterranean Sea (Vigo et 395 al., 2018a). The difference in flow direction in the CG can be related to the topography of the gulf (Figure 1) and/or to the horizontal pressure force influenced by anomalous cyclonic and 396 397 anticyclonic atmospheric conditions which were present in 2022, as found in Marullo et al. (2023). These atmospheric conditions could also be potential causes of the different seasonal geostrophic 398 399 patterns shown in Figure 6 and 7. The influence of tides can also be found in the difference of the seasonally averaged KE computed in the case of full SSH and detided SSH. In winter, in the case of 400 geostrophic currents computed from full SSH, the KE can reach ~50 cm²/s², while it decreases in 401 402 the other seasons with the lowest values detected in summer/fall (KE <5 cm²/s²). The tides' 403 influence on geostrophic circulation can be also quantified by the differences in mean KE computed from full SSH and detided SSH fields. The largest MKE values (8.25 and 8.06 cm²/s² for tidal and 404 405 detided fields, respectively) can be observed in winter, while the lowest values are observable in 406 fall, with an average value of about 0.17/0.14 cm²/s². In spring and summer, the MKE values are 2.06/1.3 and 0.43/0.23 cm²/s², respectively. Moreover, in spring and summer the relative weight of 407 the tidal component of the KE is much stronger (46% and 37% respectively) than in winter and fall 408 409 (2% and 17%). Since tidal forcing itself does not have significant seasonal variability, it is clear that 410 it does not affect the varying seasonal patterns shown in Figures 6a, c and 7a, c. The impact of tides 411 on geostrophic circulation can be observed for the cyclonic vortex detectable in spring, summer and fall north-west of Djerba Island (~10.4°E-10.9°E and ~33.8°N-34.15°N, see the red lines in Figures 6 412 and 7) in the full SSH field, which disappears when deriving geostrophic circulation from detided 413 414 SSH fields.

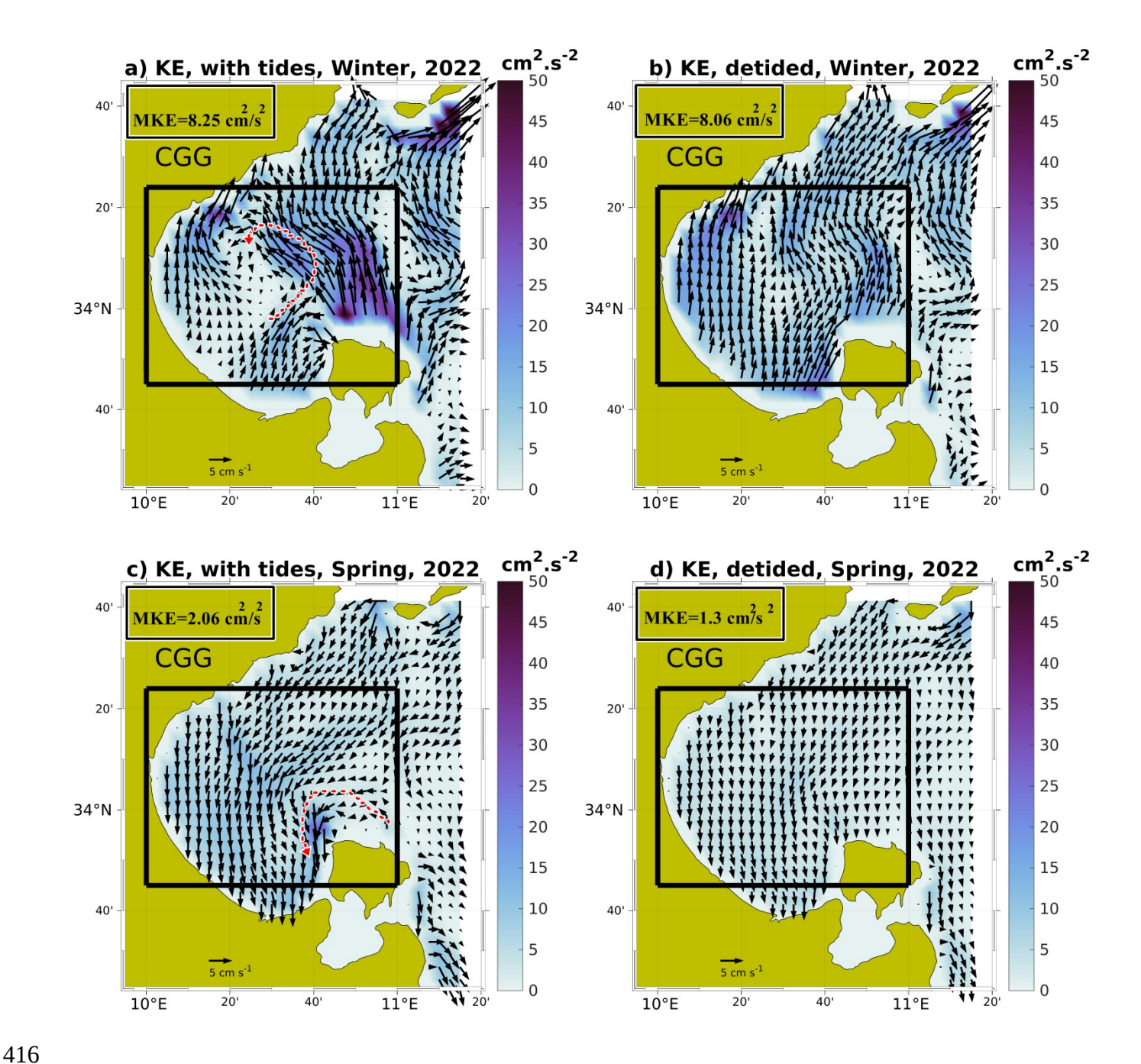


Figure 6: Seasonal mean geostrophic currents computed from MEDSEA_ANALYSISFORECAST_PHY_006_013 product SSH fields; both native with tidal forcing included (a, c) and detided (b, d) superimposed to seasonal Mean Kinetic Energy (MKE), in winter and spring, for the year 2022. The average MKE values are shown in the inserts. The black rectangles show the CGG while the dashed red lines show the cyclonic currents.

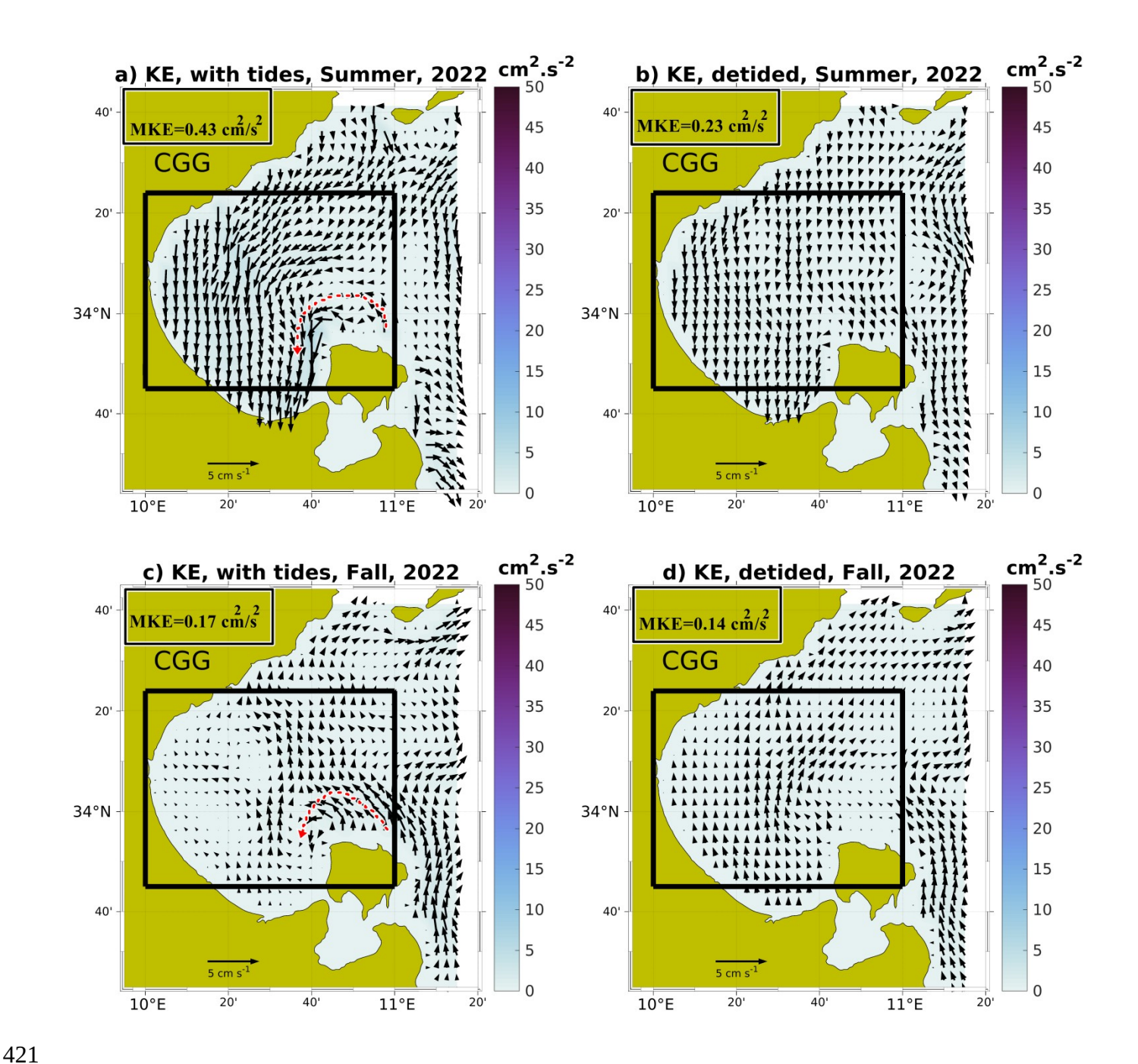


Figure 7: Seasonal mean geostrophic currents computed from MEDSEA_ANALYSISFORECAST_PHY_006_013 product SSH fields; both native with tidal forcing included (a, c) and detided (b, d) superimposed to seasonal Mean Kinetic Energy (MKE), in summer and fall for the year 2022. The average MKE values are shown in the inserts. The black rectangles show the CGG while the dashed red lines show the cyclonic currents.

We quantified the impact of tides on the dynamics of the CGG by computing the normalized Okubo-Weiss parameter Q* (eq. 6) from the geostrophic currents derived from the model SSH fields in 2022. The results are displayed in Figures 8 a, c and 9a, c for the full signal and Figures 8 b, d and 9b,d for the tidal residual. Analyzing the geostrophic circulation derived from full SSH fields in the CGG, the study area can be classified as a hyperbolic region throughout all the seasons, with a value of Q* clearly close to 1 for most of the time (>90%), due to strong deformation

gradients. On the contrary, the diminished effect of rotation on CGG topology can be clearly observed for a small portion of the study area (<8%), where values of Q* are close to -1.

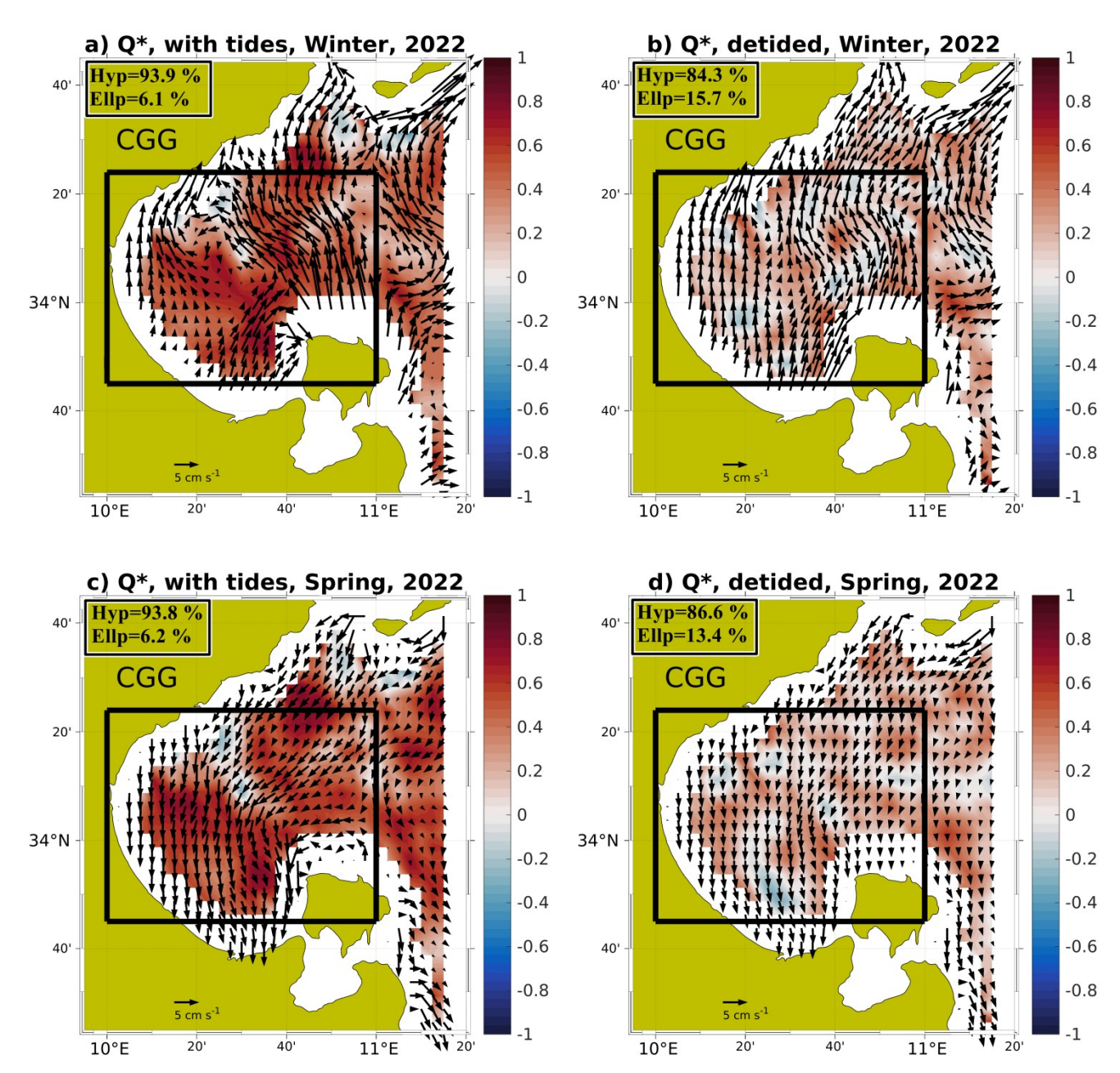


Figure 8: Seasonal mean normalized Okubo-Weiss parameter Q* with superimposed mean geostrophic currents computed from MEDSEA_ANALYSISFORECAST_PHY_006_013 product SSH fields, both native with tidal forcing included (a, c) and detided (b, d), in winter and spring for the year 2022. The inserts show the percentage of the domain where Q*<0 (elliptic grid cells) and Q*>0 (hyperbolic grid cells). The black rectangles show the CGG.

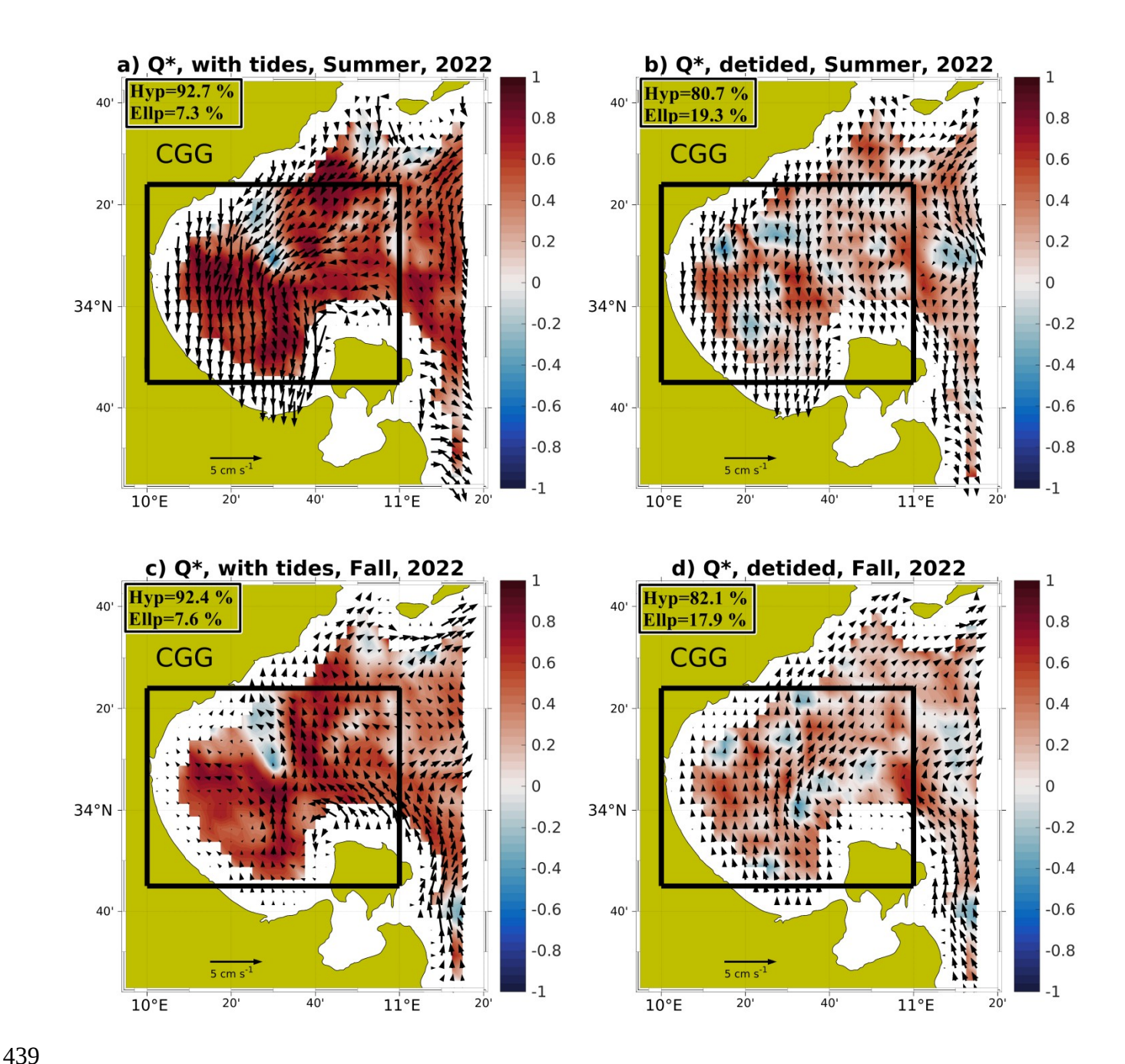


Figure 9: Seasonal mean normalized Okubo-Weiss parameter Q* with superimposed mean geostrophic currents computed from MEDSEA_ANALYSISFORECAST_PHY_006_013 product SSH fields, both native with tidal forcing included (a, c) and detided (b, d), in summer and fall for the year 2022. The inserts show the percentage of the domain where Q*<0 (elliptic grid cells) and Q*>0 (hyperbolic grid cells). The black rectangles show the CGG.

The highest elliptic grid cell percentages were detected in summer (7.3%) and fall (7.6%) where the

The highest elliptic grid cell percentages were detected in summer (7.3%) and fall (7.6%) where the flow becomes more meandering than in winter and spring. By removing the tidal signal from SSH fields a decrease of \sim 10% of the hyperbolic areas (Figures 8 b, d and 9b, d) can be observed. In contrast, an increase of \sim 10% of elliptic regions can be noticed, with the flow becoming meandering. In general, the CGG is dominated by hyperbolic regions, and the presence of tides clearly enhances this tendency by approximately 10%. A possible explanation of the dominating

hyperbolic structures even in the case of absence of tides might be related to the impact of wind on geostrophic circulation. Similar results were found in the Black Sea (Bouzaiene et al., 2021) where the hyperbolic regions are strongly dominant in winter due to larger wind stress, while in summer the elliptic areas are more pronounced because of the meandering currents.

3.2.2 Impact of tides on strain and effect on biogeochemical distribution

450

451

452

453

454

455

456

457

458

459

460

461

462 463

464

465

466

467

468

469

In order to confirm that tidal forcing is amplifying the deformation rate S* that could increase the recorded hyperbolic grid cells found in Figures 8 and 9, we computed the normalized deformation rate both from full SSH (case 1) and detided SSH (case 2) fields and the corresponding time series are shown in Figure 10. In the presence of tides (blue dots) the S* is larger than in the absence of tides (red dots) throughout the entire considered period. The difference between S* in the two cases (yellow has average of approximately 0.1 dots) meaning that tides stretching/deformation rates in the CGG and potentially enhance the presence of hyperbolic regions.

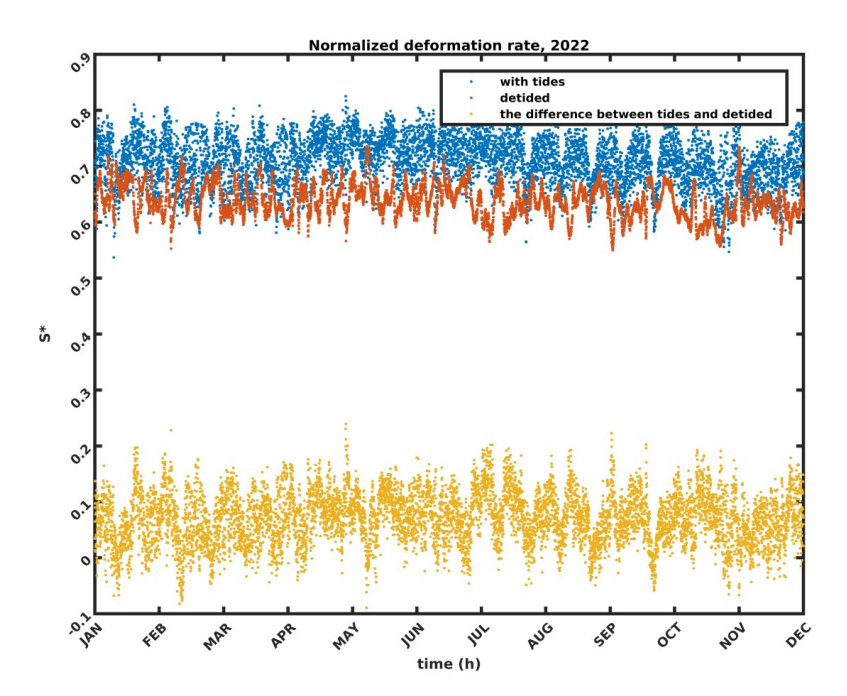


Figure 10: Time series of the deformation rate (S*) computed from MEDSEA_ANALYSISFORECAST_PHY_006_013 product in 2022: full SSH fields (blue curve), detided SSH fields (red curve) and their difference (yellow curve).

To investigate the influence of tides on CGG turbulence, the Probability Density Function (PDF) of the normalized vorticity (ζ^*) has been computed on a seasonal basis in the two different cases mentioned above and the results are shown in Figure 11. In the case of a 2D theoretical isotropic and homogeneous turbulent flow, the PDF shows a Gaussian shape without intermittency (absence of tails).

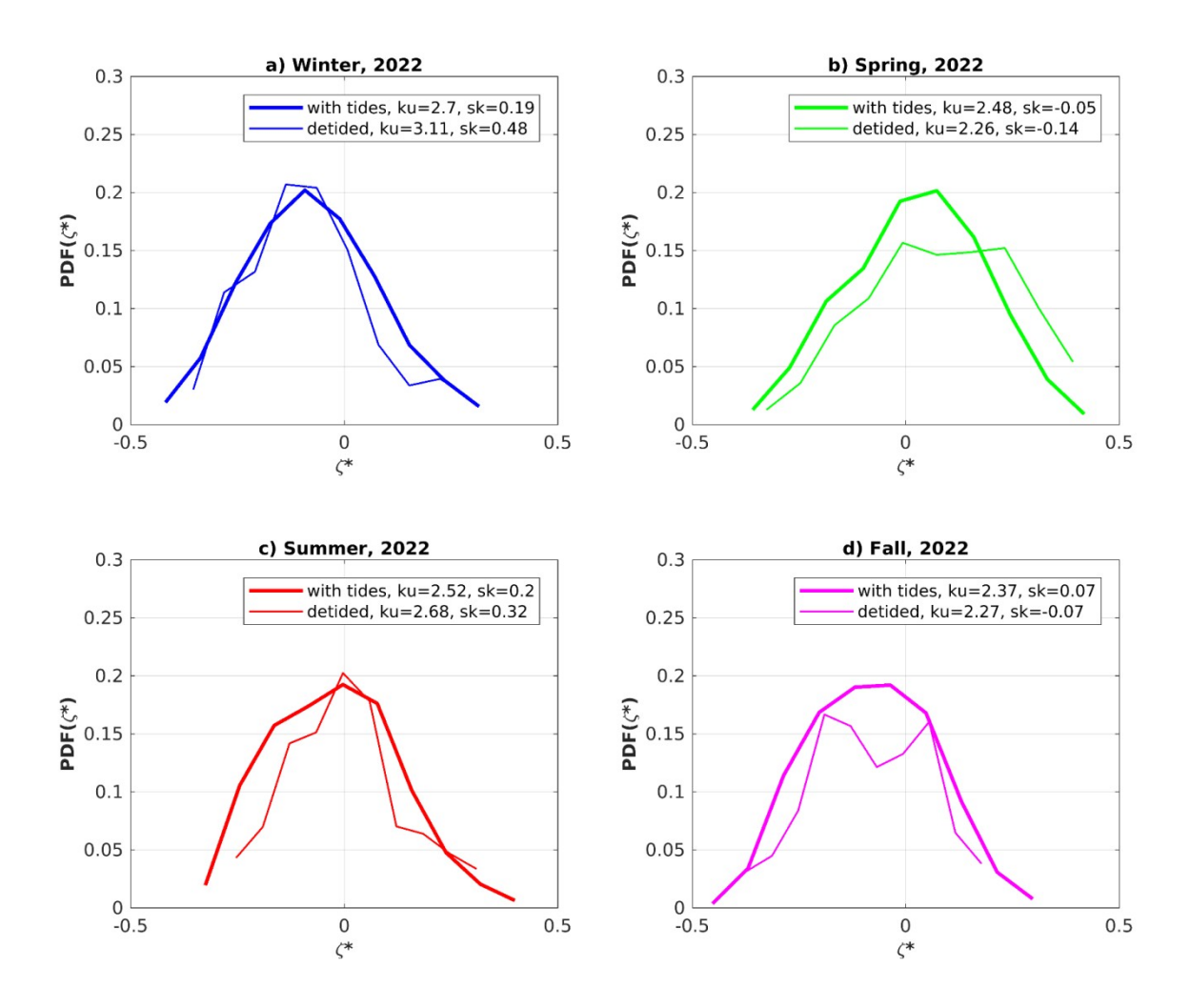


Figure 11: Seasonal Probability Density Function (PDF) of normalized vorticity (ζ*) computed from MEDSEA_ANALYSISFORECAST_PHY_006_013 product in 2022: full SSH fields (bold curves) and detided SSH fields (thin curves) in (a) winter, (b) spring, (c) summer and (d) fall.

5

In our study the PDFs exhibit nearly Gaussian shapes. These appear to be regular shapes for all the seasons in case of flow affected by tides, with observable intermittency (long tails, ~-0.4 to 0.4) associated with the presence of coherent structures. The first case (SSH fields including tides) is well known as 2D quasi-geostrophic turbulence. Different Kurtosis and Skewness values depending on the season have been found. Low skewness values were detected in spring (sk=-0.05) and in fall (sk=0.07). Larger values were found in winter (sk=0.19) and summer (sk=0.2), with corresponding Kurtosis values of 2.48, 2.37, 2.7 and 2.52, respectively. The difference in Skewness and Kurtosis is essentially due to: (1) non-homogenous and anisotropic turbulent flow, (2) the influence of coherent vortices, (3) the presence of stretching/deformation. The anisotropic flow for asymmetric PDFs may be due to the asymmetry in flood and ebb tidal currents (Song, et al., 2007). For the 2nd

case (i.e., the non-tidal forcing CGG dynamic) the shapes of all the normalized vorticity PDFs are irregular.

487

488

489

490

491

492

493

494

495

496

497

498

499

500

501

502

503504

505

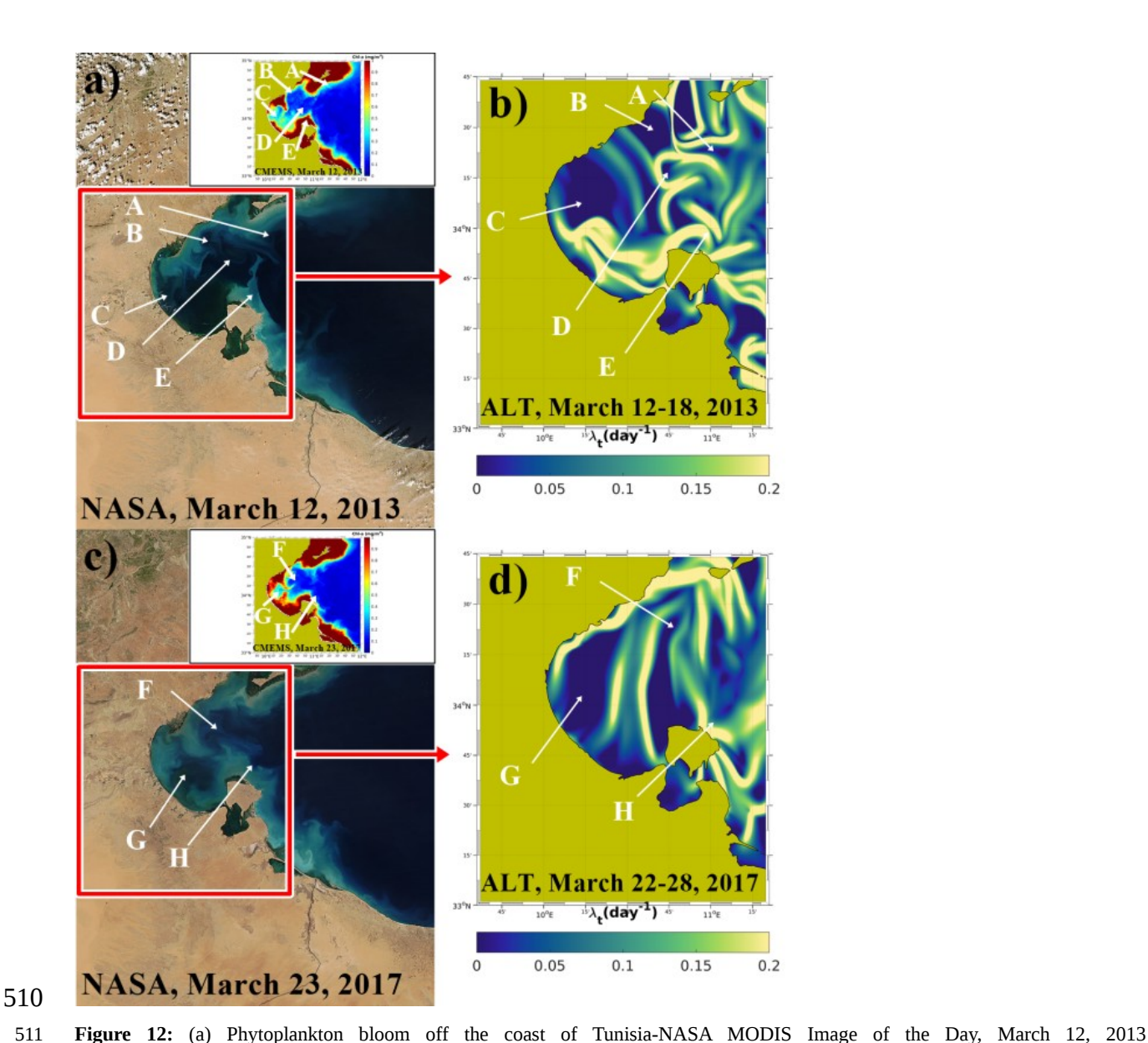
506

507

508

509

The central part of the GG is dominated by the presence of cyclonic eddies where the divergence is mostly positive as shown in Figure 4. The dynamics in the central GG region, as shown through the analysis of the altimetry data, is very different with respect to its northern and southern subareas, where prominent filaments and upwelling currents enhance phytoplankton blooms. Furthermore, the CGG, as shown through model data analysis, is rich in tidal activity, leading to the generation of cyclonic currents and relevant hyperbolic regions characterized by shearing and stirring oceanic flows. The tidal perturbation may impact the mixed layer, promoting upwelling processes that supply nutrients to the euphotic zone. The dispersion of phytoplankton blooms, when compared to FTLE, exemplifies how metrics like FTLE can be used to demonstrate the physical control on biogeochemical dispersion. One of the possible applications of the results of our work is the study of the dispersion of nutrients connected to phytoplankton bloom events that occurred in the GG and captured by NASA satellite images in March 2013 and 2017 as shown in Figure 12. The concept behind this application is to enhance the knowledge on how physics drives biogeochemistry: by comparing the phytoplankton blooms to the λ_t integrated over 7 days for high resolution of initial particle grid positions of 1/128°, this method may effectively enhance our comprehension of the link between physical processes and biogeochemistry. The qualitative correlation between algal bloom and λ_t shows how the latter can be used as a proxy for the distribution of the biomass and nutrients within the gulf. The positive divergence detected in the central Gulf of Gabès (Fig. 4b) explains the tendency to upwelling in this area (Poulain, 1993). The surface chlorophyll concentration from CMS multi-satellite observations at 1 km resolution is displayed in the inserts of Figure 12 along with the phytoplankton blooms captured from NASA (March 12, 2013, March 23, 2017). A link between physics (FTLE) and biogeochemistry (Chl-a bloom) is noticeable, with the Chl-a being dispersed on the edges of the GG coherent structures.



513

514

515

516

517

518

519

520

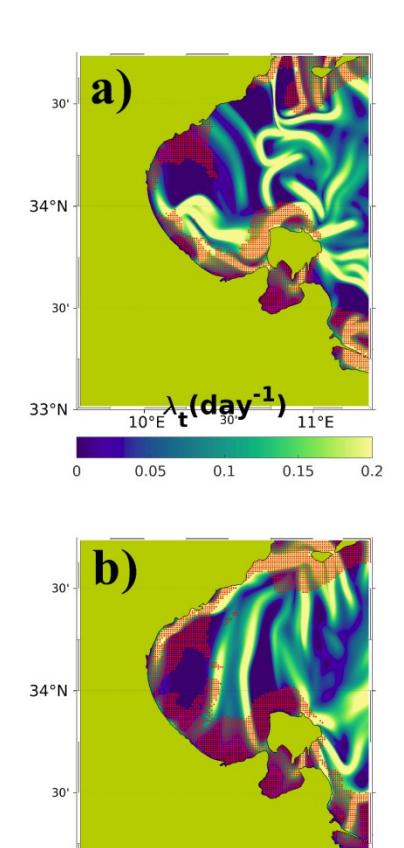
521

522

523

(https://modis.gsfc.nasa.gov/). (b) Spatial distribution of λ_t from computed altimetry (SEALEVEL_EUR_PHY_L4_MY_008_068) for 12-18 March 2013. (c) Phytoplankton blooms in the GG from NASA on March 23, 2017 and (d) spatial distribution of FTLE for 22-28 march 2017. Labels as A, B, C, D, E, F, G, H denote the features detected by NASA. In the insets we show chlorophyll a concentration from the European Union-Copernicus Marine Service (2022) for the same period as phytoplankton blooms were captured by NASA. This area is therefore the natural location for a high concentration of nutrients, favored also by the presence of cyclones (Salgado-Hernanz et al, 2019). GG features appear as transport barriers for phytoplankton dispersion. The phytoplankton blooms are driven by fronts, filaments, and mesoscale structures labeled as A, B, C, D, E, F, G and H in Fig. 9. A similar scenario has been observed in the northeastern Atlantic Ocean, where phytoplankton spring blooms are modulated by the mesoscale dynamics (Lehahn, et al., 2007). It has been found in some cases that FTLE/FSLE can show fronts producing Chl-a filaments controlling phytoplankton bloom (Lehahn, et al., 2007; Guinder et al, 2025) and $λ_t$ can be used as a good indicator of phytoplankton blooms.

Starting from the hypothesis adopted in Suthers et al. (2023), i. e. that frontal eddies interacting with boundary currents may provide a suitable offshore nursery habitat, we filtered the OCEANCOLOUR_MED_BGC_L4_MY_009_144 dataset in order to define the areas of the domain with Chl-a concentration larger than 0.6 mg/m³. Then we superimposed these areas on the FTLE fields for the same aforementioned phytoplankton bloom events in 2013 and 2017 (see Figure 13). Large amounts of Chl-a were dispersed into GG frontal boundary eddies in both cases. Therefore, the GG coastal fronts appear to be the most significant driver for phytoplankton blooms dispersion. FTLE can explain the relative 2D horizontal dispersion/distribution of some biological quantities and thus provide some insights on potential vertical processes that may engender phytoplankton blooms (Lévy et al., 2018).



0.05

Figure 13: (a) Spatial distribution of λ_t computed from altimetry data (SEALEVEL_EUR_PHY_L4_MY_008_068) for 12-18 March 2013 superimposed with chlorophyll a concentration (Chl-a >0.6 mg/m³, red dotted areas), from the European Union-Copernicus Marine Service (2022) for 12 March 2013. (b) Spatial distribution of λ_t computed from altimetry data (SEALEVEL_EUR_PHY_L4_MY_008_068) for 22-28 March 2017 superimposed with chlorophyll a concentration (Chl-a >0.6 mg/m³, red dotted areas) from the European Union-Copernicus Marine Service (2022) for 23 March 2017.

0.15

4 Summary and conclusions

In this work the main hydrodynamic features of the Gulf of Gabès were investigated by means of geostrophic velocities derived from 30 years of satellite altimetry data and 1 year (2022) of hourly 544 545 SSH fields produced by a high-resolution oceanographic numerical system. Altimetry analysis of the GG is presented in terms of normalized vorticity (ζ^*), normalized divergence (δ^*), normalized 546 547 Okubo-Weiss (Q*), normalized deformation (S*) and FTLE (λ_t), to have an overview of the main circulation features (and their seasonal variability) of the GG. The mean spatial distribution of λ_t 548 549 (1993-2022) confirms the presence of well-known features in the study area, such as ATC, MG, SMG and LSBV. The signature of these features can be found in the intensity of λ_t (Fig. 2b). The 550 551 FTLE is a powerful diagnostic tool for ocean turbulence and horizontal mixing/stirring. It often 552 varies inversely with phytoplankton concentration as it can act as a barrier to offshore transport 553 (Hernandez-Garcia et al., 2010). This may explain the poverty in nutrients in regions relatively far from the GG where we detected high values of λ_t , and it is in agreement with the known high 554 biological production in areas close to the coast, where we found low values of λ_t . This study 555 556 investigates sea surface height trends over the GG from 1993 to 2022, where the surface layer 557 shows a speed trend of 0.033 cm/s and a KE trend of 0.34 cm²/s² as shown in Figure 3. The evolution of regional dynamics, and the consequent potential impact on biogeochemical aspects, is 558 certainly a highly interesting topic, worthy of further investigation in future studies. 559 560 The different statistics show the presence of three different dynamical areas close to the GG coastal 561 zones; North Gulf of Gabès (NGG), Central Gulf of Gabès (CGG) and Southern Gulf of Gabès 562 (SGG). 563 The CGG subarea can be considered a zone rich in nutrients (since δ^* showed some positive values) 564 where the flow tends to spread particles. This scenario is observed for some seasons, with the divergence positive curve indicating the divergence of the CGG flow and explaining the 565 566 phytoplankton blooms previously observed by Feki-Sahnoun et al. (2018). Furthermore, in the coastal zones located in the NGG the flow tends to be neutral ($\delta^*\sim 0$), except for some seasons when 567 568 δ^* is larger than zero, maybe due to the presence of upwelling events close to Djerba Island. In 569 contrast, in the SGG, the flow is convergent, since it is characterized by a negative value of δ^* . In 570 this latter case the vorticity is concomitantly negative due to the signature of an anticyclonic vortex. 571 Geostrophic coastal currents and eddies are associated with the presence of hyperbolic regions 572 $(Q^*>0)$ in any season, with a crucial role played by stretching/deformation gradients (Figs $\frac{4}{5}$). Satellite observations are limited in the CGG, especially close to the boundaries, not allowing to 573 574 study tidal signal impact on geostrophic circulation. We used a high resolution model data to focus 575 on tidal signal impact on geostrophic pattern and topology (i.e., the distribution of elliptic and 576 hyperbolic regions). To the best of our knowledge, this paper for the first time discusses how tides

577 affect the CGG flow topology. The flow topology has been related to anomalous absolute dispersion regimes in the Mediterranean Sea (Bouzaiene, et al., 2018) and the Black Sea (Bouzaiene, et al., 578 2021). Tides amplify hyperbolic regions in the CGG, with more than 90% of hyperbolic grid cells 579 580 (Q*>0) captured in any season, while elliptic regions almost disappear due to the outgrowth of 581 hyperbolic ones. We also observed a significant change in geostrophic circulation pattern through 582 the different seasons, as discussed in Figs. 6 and 7. These different patterns could be related to gulf 583 topography, current instability and horizontal pressure gradients influenced by other atmospheric 584 components. Waves in a coupled hydrodynamic-wave model can be an important factor affecting 585 the geostrophic field as shown by other studies (Morales-Marquez et al 2023, Ruhs et al, 2025). A 586 lower number of data observations were observed within the GG coastal areas as mentioned in 587 model QUID where the RMSD of SLA increases significantly. This discrepancy can be reduced in 588 the model itself since it was combined with data assimilation. In regions or time scales where 589 geostrophic components become significant, given that the model includes tidal forcing and wave 590 coupling, we might not be in geostrophic balance anymore. In the Mediterranean Sea, given that the 591 high resolution model includes waves and tides, it offers an accurate geostrophic circulation 592 (Escudier et al, 2021). 593 Lower MKE values are recorded in summer and autumn, while higher values are detected in winter/ 594 spring. Since marine species disperse in regions characterized by lower turbulence and less energy 595 intensity, our findings are in good agreement with the results found in Solgado Hernanz et al. 596 (2019), where enhanced chlorophyll distribution in the CGG starts in June, peaks in September and 597 terminates in February. Another finding of this study is the way tides contribute to stretching/deformation (S*) to define the signature of the hyperbolic regions. The time series of S* derived from geostrophic currents computed from the full SSH fields shows larger values with respect to the one computed from

Another finding of this study is the way tides contribute to stretching/deformation (S*) to define the signature of the hyperbolic regions. The time series of S* derived from geostrophic currents computed from the full SSH fields shows larger values with respect to the one computed from detided SSH fields. This confirms that tides are dynamically responsible for the amplification of deformation gradients. PDFs emphasize the non-homogeneity and anisotropy of the CGG turbulent flow due to the presence of eddies and intense strain factor.

To conclude, altimetry data available for the period of 1993–2022 was analyzed in the larger Gulf

To conclude, altimetry data available for the period of 1993–2022 was analyzed in the larger Gulf domain by comparing the dynamics in three subareas and defining their common characteristics. The central part of the gulf is dominated by an upwelling flow (thus characterized by divergence) where there is an important biological production rate. The other areas located in its northern and southern parts are dominated by anticyclonic structures. The three subareas can be classified as hyperbolic regions (Q*>0). The geostrophic circulation derived from altimetry data for the three decades within the GG is characterized by strong seasonal and spatial variability. Furthermore the

- dynamics varies differently in the three subareas. The high spatiotemporal resolution of model
- outputs allowed the analysis of the CGG over the year 2022. In good accordance with the altimetry
- analysis, the CGG can be classified as a hyperbolic area with a signal greater than 90%, whereas the
- signature of elliptic zones is lower than 10%. Atmospheric conditions, topography and tidal forcing
- are very important for the occurrence of hyperbolic regions driven by strain. As well as amplifying
- 616 hyperbolic regions, tides also affect the isotropy and homogeneity of the theoretical turbulent flow.
- PDF is applied to quantify the impact of tides on 2D turbulence theory and the PDF asymmetric
- 618 distributions reveal the non-homogeneity and anisotropy of the surface flow due to persistent
- 619 stretched currents and eddies.
- 620
- 621 Data availability. This study has been conducted using E.U. Copernicus Marine Service
- 622 Information. The products used are MEDSEA_ANALYSISFORECAST_PHY_006_013 (Clementi
- 623 etal.2023,
- 624 https://doi.org/10.25423/CMCC/MEDSEA_ANALYSISFORECAST_PHY_006_013_EAS8),
- 625 SEALEVEL_EUR_PHY_L4_MY_008_068 (European Union-Copernicus Marine Service 2021,
- 626 https://doi.org/10.48670/MOI-00141) and OCEANCOLOUR_MED_BGC_L4_MY_009_144
- 627 ((https://doi.org/10.48670/moi-00300, Mediterranean Sea Ocean Satellite Observations, the Italian
- 628 National Research Council (CNR Rome, Italy)) which are made available through the Copernicus
- 629 Marine Data Store (https://data.marine.copernicus.eu/products).
- 630
- 631 Author contributions. Formal analysis, conceptualization, methodology, investigation, writing –
- original draft preparation: MB. Data curation: AG. Funding acquisition: SS. Writing review and
- editing: MB, AG, DD, AFD, SS and CF. All the authors have read and agreed to the published
- 634 version of the paper.
- 635
- 636 *Funding.* This research was funded by the Italian Ministry of University and Research as part of the
- 637 NextData project.
- 638 *Competing interests.* The authors have no competing interests.
- 639
- 640 *Acknowledgments*. We thank G. Haller and K. Onu for providing the code used for FTLE
- 641 computation in this study. Special thanks to my father, I am grateful for the many years you were
- 642 my guiding star, my best gratitude to you, I will never forget your kindness and support even after
- 643 your death.

644 References

- Abdennadher, J., and Boukthir, M. (2006). Numerical simulation of the barotropic tides in the
- Tunisian shelf and the Strait of sicily. J. Mar. Syst. 63, 162–182.
- Barkan, R., Winters, K. B., & McWilliams, J. C. (2017). Stimulated imbalance and the enhancement
- of eddy kinetic energy dissipation by internal waves. Journal of Physical Oceanography, 47,
- 649 181–198. https://doi.org/10.1175/jpo-d-16-0117.1
- Barkan, R., Srinivasan, K., Yang, L., McWilliams, J. C., Gula, J., & Vic, C. (2021). Oceanic
- mesoscale eddy depletion catalyzed by internal waves. Geophysical Research Letters, 48,
- 652 e2021GL094376. https://doi. org/10.1029/2021GL094376
- 653 Bel Hassen, M., Hamza, A., Zouari, A., Drira, Z., Akrout, F., and Messaoudi, S. (2010). Temporal
- and seasonal scale variations of phytoplankton biomass control in the Gulf of Gabes. Vie et
- 655 Milieu, 60(1), 17-26.
- Ben Ismail, S., Sammari, C., Béranger, K., and Lellouche, P. (2010). Atlas des données hydro-
- logiques des côtes tunisiennes. Institut National des Sciences et Technologies de la Mer 169 pp.
- Ben Ismail, S., Sammari, C., and Béranger, K. (2015). Surface Circulation Features along the
- Tunisian Coast: Central Mediterranean Sea. 26 the IUGG General Assembly, Prague. Czech
- Republic June 22 July 2.
- Ben Ismail S, Costa E, Jaziri H, Morgana S, Boukthir M, Ben Ismail MA, Minetti R, Montarsolo A,
- Narizzano R, Sammari C, Faimali M and Garaventa F (2022) Evolution of the Distribution and
- Dynamic of Microplastic in Water and Biota: A Study Case From the Gulf of Gabes (Southern
- Mediterranean Sea). Front. Mar. Sci. 9:786026. doi: 10.3389/fmars.2022.786026
- Béjaoui, B., Ismail, S. B., Othmani, A., Hamida, O. B. A. B. H., Chevalier, C., Feki-Sahnoun, W., et
- al. (2019). Synthesis review of the Gulf of Gabes (eastern Mediterranean Sea, Tunisia):
- morphological, climatic, physical oceanographic, biogeochemical and fisheries features. Estuar.
- 668 Coast. Shelf Sci. 219, 395–408. doi: 10.1016/j.ecss.2019.01.006
- 669 Blazevski, D., and Haller, G. (2014). Hyperbolic and elliptic transport barriers in three-dimensional
- 670 unsteady flows. Physica D, 273, 46–62.
- Bouzaiene M., Menna M., Poulain P-M., Bussani A., and Elhmaidi D. (2020). Analysis of the
- Surface Dispersion in the Mediterranean Sub-Basins. Front. Mar. Sci. 7:486.doi:
- 673 10.3389/fmars.2020.00486
- Bouzaiene, M., Menna, M., Poulain, P.-M., and Elhmaidi, D. (2018). Lagrangian dispersion
- characteristics in the Western Mediterranean. J. Mar. Res. 76, 139–161.
- 676 Bouzaiene, M., Menna, M., Elhmaidi, D., Dilmahamod, A-F., and Poulain, P-M. (2021). Spreading

- of Lagrangian Particles in the Black Sea: A Comparison between Drifters and a High-Resolution
- Ocean Model, Remote Sensing 13, no. 13: 2603. https://doi.org/10.3390/rs13132603
- Bower, A. S. (1991). A simple kinematic mechanism for mixing fluid parcels across a meandering
- jet. Journal of Physical Oceanography, 21(1), 173–180.
- 681 Clementi, E., Pistoia, J., Delrosso, D., Mattia, G., Fratianni, C., Storto, A., et al. (2017a). A 1/24
- degree resolution Mediterranean analysis and forecast modelling system for the Copernicus
- Marine Environment Monitoring Service. Extended abstract to the 8th EuroGOOS Conference,
- 684 Bergen.
- 685 Clementi, E., Drudi, M., Aydogdu, A., Moulin, A., Grandi, A., Mariani, A, et al. (2023).
- Mediterranean Sea Physical Analysis and Forecast (CMS MED-Physics, EAS8 system) (Version
- 1) [Data set]. Copernicus Marine Service (CMS).
- https://doi.org/10.25423/CMCC/MEDSEA_ANALYSISFORECAST_PHY_006_013_EAS8
- 689 Corti G., Cuffaro M., Doglioni C., Innocenti F., and Manetti P. (2006). Coexisting geodynamic
- 690 processes in the Sicily Channel. In: Y. Dilek & S. Pavlides (Eds), Postcollisional tectonics and
- magmatism in the Mediterranean region and Asia. Geol. Soc. Am. Spec. Paper, 409: 83-96.
- d'Ovidio, F., De Monte, S., Alvain, S., Dandonneau, Y. and Lévy, M. (2010). Fluid dynamical
- 693 niches of phytoplankton types. Proceedings of the National Academy of Sciences, 107(43),
- 694 pp.18366- 18370.
- 695 Du Toit, P. C. (2010). Transport and separatrices in time-dependent flows (PhD thesis). Pasadena,
- 696 CA: California Institute of Technology. Retrieved from
- 697 http://resolver.caltech.edu/CaltechTHESIS:10072009-165901284
- 698 Elhmaidi, D., Provenzale, A., and Babiano, A. (1993). Elementary topology of the two-dimensional
- 699 turbulence from a Lagrangian view-point and single particle dispersion. J. Fluid Mech., 257,
- 700 533–558
- 701 European Union-Copernicus Marine Service. (2021). EUROPEAN SEAS GRIDDED L4 SEA
- 702 SURFACE HEIGHTS AND DERIVED VARIABLES REPROCESSED (1993-ONGOING)
- [dataset]. Mercator Ocean International. https://doi.org/10.48670/MOI-00141
- European Union-Copernicus Marine Service. (2022). Mediterranean Sea, Bio-Geo-Chemical, L4,
- monthly means, Daily gap free and climatology Satellite Observations (1997-ongoing) [dataset].
- Mercator Ocean International. https://doi.org/10.48670/MOI-00300
- 707 Escudier R, Clementi E, Cipollone A, Pistoia J, Drudi M, Grandi A, Lyubartsev V, Lecci R,
- Aydogdu A, Delrosso D, Omar M, Masina S, Coppini G and Pinardi N (2021) A High Resolution
- Reanalysis for the Mediterranean Sea. Front. Earth Sci. 9:702285 doi: 10.3389/feart.2021.702285
- 710 Farazmand, M., and Haller, G. (2012). Computing Lagrangian coherent structures from their

- variational theory. Chaos: An Interdisciplinary Journal of Nonlinear Science, 22(1)
- Guinder, V. A., Tillmann, U., Rivarossa, M., Ferronato, C., Ramírez, F. J., Krock, B., Gu, H., and
- Saraceno, M. (2025). Extraordinary bloom of toxin-producing phytoplankton enhanced by strong
- etention on the offshore Patagonian shelf, Biogeosciences, 22, 3397–3428,
- 715 <u>https://doi.org/10.5194/bg-22-3397-2025.</u>
- Haller, G. (2002). Lagrangian coherent structures from approximate velocity data. Physics of
- 717 Fluids, 14(6)
- 718 Haller, G. (2015). Lagrangian Coherent Structures. Annual Review of Fluid Mechanics, 47(1)
- 719 Hernández-García, E., Bettencourt, J., Garcon, V. Lopez, C., Rossi, V., Sudre, J., et al. (2010).
- 720 Biological Impact of Ocean Transport: A Finite-Size Lyapunov Characterization.
- 721 10.13140/2.1.4392.7048.
- 722 IOC. (1985). Manual on Sea Level Measurement and Interpretation. Inter governmental
- Oceanographic Commission, Manuals and Guides, 14, vol. I. Basic procedures, p. 75. Available
- online at: https://www.psmsl.org/train_and_info/training/manuals/.
- Jouini, M., Béranger, K., Arsouze, T.J., Beuvier, S., Thiria, M., Crepon, I., and Taupier-Letage, I.
- 726 (2016). The Sicily Channel surface circulation revisited using a neural clustering analysis of a
- high-resolution simulation. J. Geophys. Res. Ocean. 121, 4545–4567.
- Kotta, D., and Kitsiou, D. (2019). Chlorophyll in the Eastern Mediterranean Sea: Correlations with
- 729 Environmental Factors and Trends. Environments, 6, 98.
- 730 https://doi.org/10.3390/environments6080098
- Lévy, M., FranksP. J., and Smith, K. S. (2018). The role of submesoscale currents in structuring
- marine ecosystems. Nature communications, 9 (1), 4758.
- 733 Liu, Y., Wilson, C., Green, M. A., and Hughes, C. W. (2018). Gulf Stream transport and mixing
- processes via coherent structure dynamics. Journal of Geophysical Research: Oceans, 123, 3014–
- 735 3037. https://doi.org/10.1002/2017JC013390
- Rousselet, L., Francesco d'Ovidio, Lloyd Izard, Alice Della Penna, Anne Petrenko, et al. (2024).
- A Software Package for an Adaptive Satellite-based Sampling for Oceanographic cruises
- 738 (SPASSOv2.0). tracking fine scale features for physical and biogeochemical studies. (hal-
- 739 04705438)
- 740 Macias, D., Garcia-Gorriz, E. and Stips, A. (2018), Major fertilization sources and mechanisms for
- Mediterranean Sea coastal ecosystems. Limnol. Oceanogr., 63: 897-914.
- 742 https://doi.org/10.1002/lno.10677
- 743 Marullo, S., Serva, F., Iacono, R., Napolitano, E., di Sarra, A., Meloni, D. (2023). Record-breaking
- persistence of the 2022/23 marine heat wave in the Mediterranean Sea. Environ. Res. Lett. 18

- 745 114041. 10.1088/1748-9326/ad02ae
- Menna, M., Poulain, P.-M., Ciani, D., Doglioli, A., Notarstefano, G., Gerin, et al. (2019). New
- Insights of the Sicily Channel and Southern Tyrrhenian Sea Variability. Water, 11, 1355.
- 748 https://doi.org/10.3390/w11071355
- 749 Meyerjürgens, J., Ricker, M., Schakau, V., Badewien, T. H., & Stanev, E. V. (2020). Relative
- dispersion of surfacedrifters in the North Sea: The effect offides on mesoscale diffusivity. Journal
- of Geophysical Research: Oceans, 125,e2019JC015925. https://doi.org/10.1029/2019JC01592
- 752 Millot, C., and Taupier-Letage, I. (2005). Circulation in the Mediterranean Sea. In: Saliot, A. (eds)
- 753 The Mediterranean Sea. Handbook of Environmental Chemistry, vol 5K. Springer, Berlin,
- 754 Heidelberg. https://doi.org/10.1007/b107143
- 755 Morales-Márquez, V., Hernández-Carrasco, I., Fox-Kemper, B., and Orfila, A. (2023). Ageostrophic
- contribution by the wind and waves induced flow to the lateral stirring in the Mediterranean Sea.
- Journal of Geophysical Research: Oceans, 128, e2022JC019135. https://doi.
- 758 org/10.1029/2022JC019135
- 759 Okubo, A. (1970). Horizontal dispersion of floating particles in the vicinity of velocity singularities
- such as convergence. Deep Sea Res.Oceanogr. Abstr., 17, 445–454.
- Onu, K., Huhn, F., and Haller, G. (2015). LCS Tool: A computational platform for Lagrangian
- 762 coherent structures, Journal of Computational Science, Volume 7, Pages 26-36, ISSN 1877-
- 763 7503,https://doi.org/10.1016/j.jocs.2014.12.002.
- 764 Othmani, A., Béjaoui, B., Chevalier, C., Elhmaidi, D., Devenon, J.L., and Aleva, L. (2017). High-
- resolution numerical modelling of the barotropic tides in the Gulf of Gabes, eastern
- Mediterranean Sea (Tunisia). J. Afr. Earth Sci. 129, 224–232
- Peng, Y., Xu X., Shao, Q., Weng, H., Niu, H., Li, Z., Zhang, C., Li, P., Zhong, X., Yang, J. (2024).
- Applications of Finite-Time Lyapunov Exponent in detecting Lagrangian Coherent Structures for
- 769 coastal ocean processes: a review. Front. Mar. Sci.11:1345260. doi: 10.3389/fmars.2024.1345260
- Pinardi, N., Zavatarelli M., Adani M., Coppini G. Fratianni C., Oddo P., et al. (2015),
- 771 Mediterranean Sea large-scale low-frequency ocean variability and water mass formation rates
- from 1987 to 2007: A retrospective analysis, Progress in Oceanography, Volume 132, Pages 318-
- 332, ISSN 0079-6611, https://doi.org/10.1016/j.pocean.2013.11.003.
- Poulain, P.M., and Zambianchi, E. (2007). Surface circulation in the central Mediterranean Sea as
- deduced from Lagrangian drifters in the 1990s. Cont. Shelf Res. 27, 981–1001.
- Poulain, P.-M. (1993). Estimates of horizontal divergence and vertical velocity in the equatorial
- 777 Pacific. J. Phys. Oceanogr., 23, 601–607.

- Poulain, P.-M., Centurioni, L., Brandini, C., Taddei, S., Berta, M., and Menna, M.: Relative
- dispersion and kinematic properties of the coastal submesoscale circulation in the southeastern
- 780 Ligurian Sea, Ocean Sci., 19, 1617–1631, https://doi.org/10.5194/os-19-1617-2023, 2023.
- 781 Poulain, P.-M., Menna, M., and Mauri, E. (2012b). Surface geostrophic circulation of the
- Mediterranean Sea derived from drifter and satellite altimeter data. J. Phys. Oceanogr. 42, 973–
- 783 990. doi: 10.1175/JPO-D-11-0159.1
- Rossi, V., Lopez, C., Sudre, J., Hernández-García, E., Garçon, V. (2008). Comparative study of
- mixing and biological activity of the Benguela and Canary upwelling systems. Geophysical
- 786 Research Letters, 35 (11), pp.L11602. ff10.1029/2008GL033610ff. ffhal-02296657
- Rühs, S., van den Bremer, T., Clementi, E., Denes, M. C., Moulin, A., and van Sebille, E. (2025).
- Non- negligible impact of Stokes drift and wave-driven Eulerian currents on simulated surface
- particle dispersal in the Mediterranean Sea, Ocean Sci., 21, 217–240, 21-217-doi.org/10.5194/os-
- 790 2025.
- Rypina, I. I., Pratt, L. J., and Lozier, M. S. (2011). Near-surface transport pathways in the North
- Atlantic Ocean: Looking for through put from the subtropical to the subpolar gyre. Journal of
- 793 Physical Oceanography, 41(5), 911–925.
- 794 Salgado-Hernanz, P.M., Racault, M.-F., Font-Muñoz, J.S., Basterretxea, G. (2019). Trends in
- 795 phytoplankton phenology in the Mediterranean Sea based on ocean-colour remote sensing,
- Remote Sensing of Environment, Volume 221, Pages 50-64, ISSN 0034-4257,
- 797 https://doi.org/10.1016/j.rse.2018.10.036
- 798 Sahnoun, W-F., Njah, H., Hamza, A., Barraj, N., Mahfoudi, M., Rebai, A., et al. (2017). Using
- 799 general linear model, Bayesian Networks and Naive Bayes classifier for prediction of
- 800 Kareniaselliformis occurrences and blooms, Ecological Informatics, Volume 43, 2018, Pages 12-
- 801 23, ISSN 1574-9541, https://doi.org/10.1016/j.ecoinf.2017.10.017.
- 802 Shadden, S-C., Lekien, F., Marsden, J-E. (2005). Definition and properties of Lagrangian coherent
- structures from finite-time Lyapunov exponents in two-dimensional a periodic flows. Physica D:
- Nonlinear Phenomena, 212(3-4)
- 805 Song, D., Wang, X. H., Kiss, A. E., and Bao, X. (2011). The contribution to tidal asymmetry by
- different combinations of tidal constituents, J.Geophys. Res., 116, C12007,
- 807 doi:10.1029/2011JC007270
- 808 Sammari, C., Koutitonsky, V., and Moussa, M. (2006). Sea level variability and tidal resonance in
- the Gulf of Gabes, Tunisia. Cont. Shelf Res. 26, 338–350.
- 810 Sammari, C., Millot, C., Taupier, Letage, I., Stefani, A., Brahim, M. (1999). Hydrological
- characteristics in the Tunisia-Sardinia-Sicily area during spring 1995. Deep-Sea Res. I46, 1671–

- 812 1703
- 813 Sorgente, R., Olita, A., Oddo, P., Fazioli, L., and Ribotti, A. (2011). Numerical simulation and
- decomposition of kinetic energy in the Central Mediterranean: insight on mesoscale circulation
- and energy conversion. Ocean. Sci. 7, 503–519.
- 816 Siegelman, L., 2020: Energetic Submesoscale Dynamics in the Ocean Interior. J. Phys. Oceanogr.,
- 817 50, 727–749, https://doi.org/10.1175/JPO-D-19-0253.1.
- 818 Srinivasan, M., Tsontos, V. (2023). Satellite Altimetry for Ocean and Coastal Applications: A
- 819 Review. Remote Sens. 202., 15, 3939. https://doi.org/10.3390/rs15163939
- 820 Suthers, I.M., Schaeffer, A., Archer, M., Roughan, M., Griffin, D.A., Chapman, C.C., Sloyan, B.M.
- and Everett, J.D. (2023), Frontal eddies provide an oceanographic triad for favorable larval fish
- habitat. Limnol Oceanogr, 68: 1019-1036. https://doi.org/10.1002/lno.12326
- 823 Taburet, G., Sanchez-Roman, A., Ballarotta, M., Pujol, M., Legeais, J., Fournier, et
- al. (2019). Duacs dt2018: 25 years of reprocessed sea level altimetry products. Ocean
- 825 Science, 15, 1207–1224.
- Vigo, I., Sempere, M., Chao, B., and Trottini, M., (2018). Mediterranean Surface Geostrophic
- 827 Circulation from Satellite Gravity and Altimetry Observations. Pure and Applied Geophysics.
- 828 175. 10.1007/s00024-018-1911-0.
- 829 Vigo, M.I., García-García, D., Sempere, M.D., and Chao, B.F. (2018b). 3D Geostrophy and Volume
- Transport in the Southern Ocean. Remote Sens. 10, 715. https://doi.org/10.3390/rs10050715
- 831 Weiss, J. (1991). The dynamics of the enstrophy transfer in two dimensional turbulence. Phys. D,
- 832 48, 273–294.
- 833 Zayen, A., Sayadi, S., Chevalier, C., Boukthir, M., Ben Ismail, S., and Tedetti, M. (2020).
- Microplastics in surface waters of the Gulf of Gabes, southern Mediterranean Sea: distribution,
- composition and influence of hydrodynamics. Estuar. Coast. Shelf Sci. 242:106832. doi:
- 836 10.1016/j.ecss.2020.106832